Understanding the mechanisms behind the northward extension of the West African Monsoon during the Mid-Holocene

Marco Gaetani, Gabriele Messori, Qiong Zhang, Cyrille Flamant, Francesco S. R. Pausata

The DOI for this manuscript is doi: 10.1175/JCLI-D-16-0299.1

Understanding the mechanisms behind the northward extension of the West African Monsoon during the Mid-Holocene

Marco Gaetani (1), Gabriele Messori (2), Qiong Zhang (3), Cyrille Flamant (1), Francesco S.R. Pausata (2,4)

(1) LATMOS/IPSL, UPMC Univ. Paris 06 Sorbonne Universités, UVSQ, CNRS, Paris, France

(2) Department of Meteorology and Bolin Centre for Climate Research, Stockholm University, Stockholm, Sweden

(3) Department of Physical Geography and Bolin Centre for Climate Research, Stockholm University, Stockholm, Sweden

(4) Department of Earth and Atmospheric Sciences, University of Quebec in Montreal, Montreal (QC), Canada

Corresponding author: Marco Gaetani

Laboratoire Atmosphères, Milieux, Observations Spatiales, LATMOS-IPSL

Université Pierre et Marie Curie

Boite 102, Tour 45, 3eme Etage, Couloir 45-46

4 Place Jussieu, 75252 Paris Cedex 05, France

Tel: +33 1 44 27 48 72

e-mail: marco.gaetani@latmos.ipsl.fr

Abstract

Understanding the West African monsoon (WAM) dynamics in the mid-Holocene (MH) is a crucial issue in climate modelling, because numerical models typically fail to reproduce the extensive precipitation suggested by proxy evidence. This discrepancy may be largely due to the assumption of both unrealistic land surface cover and atmospheric aerosol concentration. In this study, the MH environment is simulated in numerical experiments by imposing extensive vegetation over the Sahara and the consequent reduction in airborne dust concentration. A dramatic increase in precipitation is simulated across the whole of West Africa, up to the Mediterranean coast. This precipitation response is in better agreement with proxy data, in comparison with the case in which only changes in orbital forcing are considered. Results show a substantial modification of the monsoonal circulation, characterized by an intensification of large-scale deep convection through the entire Sahara, and a weakening and northward shift (~6.5°) of the African easterly jet. The greening of the Sahara also leads to a substantial reduction in African easterly wave activity and the associated precipitation. The reorganization of the regional atmospheric circulation is driven by the vegetation effect on radiative forcing and associated heat fluxes, with the reduction in dust concentration to enhance this response. The results for the WAM in the MH present important implications for understanding future climate scenarios in the region and in teleconnected areas, in the context of projected wetter conditions in West Africa.

Key words: African humid period, African easterly waves, dust, land cover, Green Sahara, EC-Earth

1 Introduction

Understanding climate variability in West Africa is one of the most challenging issues in current climate science, from both the academic and socio-economic perspectives. Indeed, food security in West African countries is largely based on rain fed agriculture [IFAD, 2013] and is potentially vulnerable to climate variability [Sultan and Gaetani, 2016]. Precipitation in West Africa is concentrated in the boreal summer and is primarily associated with the West African Monsoon (WAM) [Nicholson, 2013]. The WAM underwent large variability in the 20th century, showing a succession of long lasting wet and dry periods following multidecadal trends [Rodríguez-Fonseca et al., 2015]. In this context, the need for reliable predictions of rainfall in West Africa on decadal and longer time scales is crucial. However, state-of-the-art climate models are still deficient in correctly reproducing the historical variability and agreeing on future projections [Biasutti, 2013]. The skill in identifying and disentangling the numerous drivers of the WAM variability that operate at different spatial and temporal scales is modest at best [Biasutti et al., 2009; Rowell, 2013].

Furthermore, climate change in West Africa has been much larger during the Holocene interglacial period than in the 20th century. Extreme droughts, developing in a matter of few years or decades, have been recorded during late Holocene (5-0 kyr BP), with dramatic lake low stands near the Equator [Shanahan et al., 2006] and the complete drying of fresh water bodies in the Sahel [Gasse, 2000]. The opposite scenario occurred during early Holocene, between 15 and 5 kyr ago, when increased summer precipitation led to an expansion of the North African lakes and wetlands and an extension of grassland and shrubland into areas that are now desert, giving origin to the so-called “Green Sahara”, or African Humid Period (AHP) [Holmes, 2008]. Model simulations for the mid-Holocene (MH, 6 kyr BP) show

limitations in reproducing the intensification and geographical expansion of the WAM precipitation [Harrison et al., 2014], and these shortcomings may be similar to those affecting historical simulations and future projections. In general, numerical simulations of the WAM dynamics are particularly sensitive to the shortcomings commonly affecting climate model physics, such as the inaccurate representation of clouds, energy fluxes, coupling at the surface, and convection at the sub-grid scale. Moreover, the coarse resolution of global climate models is insufficient to properly simulate the mesoscale convection characterizing the WAM precipitation. In historical simulations, fully coupled models exhibit biases in reproducing the tropical Atlantic dynamics, resulting in warmer SST and weaker monsoonal circulation [Roehrig et al., 2013]. In the description of future climate scenarios, the model sensitivity to the global surface warming, and to the direct CO2 radiative forcing, appears crucial for the sign of the projected precipitation trends [Giannini, 2010; Gaetani et al., 2016].

A number of studies have addressed the limitations in modelling the West African climate in the MH, pointing to Saharan land cover as the key ingredient to simulate precipitation patterns fitting paleoclimate data. By using a coupled atmosphere-vegetation model, Claussen and Gayler [1997] found an amplification of the response of the atmospheric circulation to changes in the Earth's orbit produced by a positive precipitation-vegetation feedback. By prescribing a vegetated Sahara, several authors found a good agreement between simulated precipitation and paleoclimate data, and identified the increased low-level moisture, which destabilizes the vertical column and enhances convection, as a crucial factor to maintain the intensification of the monsoon system due to the orbital forcing [Su and Neelin, 2005; Patricola and Cook, 2007; Swann et al., 2014]. The use of interactive vegetation climate models confirms the positive precipitation-vegetation feedback and the key role of the latent

heat increase in favoring the convection [Patricola and Cook, 2008; Rachmayani et al., 2015], though the importance of the decrease in surface albedo is also highlighted [Levis et al., 2004]. A recent study has shown that accounting for the large reduction in airborne dust emission is also essential for an accurate simulation of the WAM strength during the MH [Pausata et al., 2016]. The authors pointed out that the Paleoclimate Modelling Intercomparison Project (PMIP) [Braconnot et al., 2011] and the Coupled Model Intercomparison Project (CMIP) [Taylor et al., 2012] protocols specify the MH dust concentration and land cover to be equal to the pre-industrial (PI) period, which may be the main cause of the models' dry bias in simulating the MH WAM. In recent numerical experiments, the inclusion of both dynamic vegetation and dust emissions is not sufficient to reproduce an intensification of the WAM compatible with paleoclimate data, if the initial configuration for the vegetation is set to PI levels. Indeed, the simulated precipitation changes do not allow vegetation to grow north of 15° N, and the associated variations in dust load compared to PI climate are limited, and so are the feedbacks [Harrison et al., 2015].

Building upon the study of Pausata et al. [2016], this work aims to describe in detail the dynamics of the WAM during the MH, elucidating the mechanisms whereby changes in land cover and associated mineral dust emission alter atmospheric circulation and precipitation patterns. For this purpose, fully coupled climate model experiments, in which Saharan vegetation and dust concentrations are changed concomitantly and in turn, are analyzed. In the context of the existing literature on the topic, the analysis of the mineral dust's role in modifying the atmospheric dynamics under vegetated Sahara conditions represents a novel and original contribution to the understanding of the WAM system in the MH. The results of this study are particularly relevant not only from a paleoclimate perspective but also with respect to the assessment of future scenarios for West Africa [Schmidt et al., 2014]. Indeed, a

number of projections simulate a positive precipitation trend, and a subsequent land greening and dust reduction [Evan et al., 2016]. The paper is organized as follows: the climate model and the experimental design are described in section 2, the results are presented and discussed in section 3, and the main findings are summarized in section 4.

2 Model and experimental setup

In the present study, the climate simulations performed by Pausata et al. [2016], using version 3.1 of the atmosphere-ocean fully coupled climate model EC-Earth [Hazeleger et al., 2010], are analyzed. The atmospheric model is based on the Integrated Forecast System (IFS cycle 36r4) [ECMWF, 2010], including the H-TESSEL land model [van den Hurk et al., 2000]. In the land model, each grid-box is divided into fractions (bare ground, low and high vegetation, intercepted water, shaded and exposed snow are represented over land), with properties defining separate heat and water fluxes used in an energy balance equation solved for the skin temperature. A fraction of the rainfall is collected by an interception layer, where the remaining fraction is partitioned between surface runoff and infiltration. Infiltration and runoff schemes depend on the soil texture and standard deviation of orography. The simulation is run at T159 horizontal spectral resolution (~1.125°, approximately 125 km) with 62 vertical levels. The atmospheric component is coupled by the OASIS 3 coupler [Valcke, 2006] to the Nucleus for European Modelling of the Ocean version 2 (NEMO) [Madec, 2008], and the Louvain-la-Neuve Sea Ice Model version 3 (LIM3) [Vancoppenolle et al., 2008]. The ocean component NEMO has a nominal horizontal resolution of 1° and 46 vertical levels.

A control simulation (CTL) is performed following the PMIP3 protocol [Braconnot et al., 2011]. The orbital forcing is set to MH values (6 kyr BP). For the greenhouse gases, the methane is set at 650 ppb, instead of the 760 ppb PI value, and CO2 and other greenhouse gases are set to PI levels. Aerosol particle emissions, the solar constant, ice sheets, topography and coastlines are set to PI conditions. The CTL run is compared to three sensitivity experiments, which simulate the MH climate in the presence of a Green Sahara with reduced atmospheric dust concentrations (GSRD), a Green Sahara with PI dust (GSPD), and a present-day Sahara with reduced dust (PSRD).

The changes in vegetation in the GSRD and GSPD experiments are imposed by prescribing the vegetation type over the Sahara-Sahel region [11°-33°N, 15°W-35°E] to be evergreen shrub with a leaf area index (LAI) equal to 2.6. The change in vegetation cover leads to a decrease in the albedo (averaged into the Sahara-Sahel region) from 0.30 to 0.15 (Table 1). Surface roughness and soil wetness are prescribed to PI values in the sensitivity experiments. As discussed in detail in Pausata et al. [2016], the experiment design is idealized. Nevertheless, recent studies have shown that paleolakes extended at least to 28°N [Lézine et al., 2011] and tropical vegetation migrated as far as 24°N during the AHP, about 1000 km further north than today [Hély et al., 2014]. Based on leaf wax isotopes, Tierney et al. [2017] show that the Green Sahara extended all the way to the northern most part of western Sahara, with peaks in precipitation above 1000 mm/year relative to present day. Hence, proxy evidence suggests an extensive greening across the entire Sahara during the MH, overall supporting the choice of the prescribed vegetation cover in the GSRD and GSPD experiments. Furthermore, Pausata et al. [2016] have shown that changes in WAM strength do not strongly depend on the exact choice of the vegetation type prescribed over eastern Sahara, which may have experienced dryer conditions compared to the western part.

The atmospheric dust concentration is prescribed in the CTL simulation by using the PI dust climatology derived from the Community Atmosphere Model [Albani et al., 2014], which is used in the CMIP5 exercise. The size distribution of dust corresponds to diameter ranges from 0.1 to 10.0 μm. The model used in this study simulates the direct effect of dust on the atmospheric radiative balance, while the indirect effect on cloud formation and microphysics is not included. To take into account the decreased dust emission and concentration typical of the AHP, in the GSRD and PSRD experiments the PI dust concentration is reduced by 80% throughout the troposphere (up to 150 hPa) over a broad area around the Sahara desert (see Figure S1 in Pausata et al. [2016]). This choice is justified by evidence from proxy records off the coast of Morocco showing a dust flux reduction of 60-80% [deMenocal et al., 2000; McGee et al., 2013], and also supported by a recent dust modelling study [Egerer et al., 2016]. The imposed dust reduction leads to a decrease in the global dust aerosol optical depth (AOD) of almost 60% and in the total AOD of 0.02 (see Figure 1 in Pausata et al. [2016]). The PI climatological dust mixing ratio prescribed in the CTL and GSPD simulations (Figure 1a) closely represents the main features of the present-day dust distribution over North Africa, namely the peak over the Bodélé depression north of Lake Chad, and the band over western Sahara and Sahel [Ginoux et al., 2012]. An intense peak in concentration is present over eastern Sahara, largely dominating the African dust emission in summer, which appears as an artifact when compared with satellite retrievals for the present-day distribution (compare Figure 1a with Figure 4 in Ginoux et al. [2012]). This artifact affects the radiative balance simulated in the region, by masking the dust sources to the west, with potential repercussions on the simulation of the regional atmospheric dynamics. Additional simulations have been performed to test the effect of imposing a more realistic dust climatology, finding barely significant differences in the effect of dust reduction on precipitation (see Figures S1-

S3 in the Supplementary Material online). However, dust emission from the central and western Sahara is intimately linked to the surface wind pattern over North Africa, which shows a broad variability at multidecadal time scales [Evan et al., 2016]. Thus, substantial differences in the surface wind fields in the PI period could explain this apparently incongruous dust concentration pattern produced by the CAM model. However, the meridional profile of dust concentration (averaged between 15°W and 25°E, to cut the unusual peak to the east off) is close to the present-day pattern, showing a dust layer reaching the mid-troposphere, with an intense peak around 15-20°N (corresponding to the Bodélé and western Sahara sources), and a mid-tropospheric plume extending south to the Gulf of Guinea (Figures 1c, e). When the dust concentration is reduced by 80%, the highest anomalies are located where the PI concentration is maximum, namely over central and eastern Sahara, around 15-20°N, up to 800-700 hPa (Figures 1b, d, f).

In each experiment, initial conditions are taken from a 700-year PI spin-up run, and the simulations are then run for about 300 years. The quasi-equilibrium is reached after 100-200 years depending on the experiment. This study focuses on the monsoonal season (June to September, JJAS) for the last 30 years of each experiment. The experimental setup is summarized in Table 1, and a detailed description is presented in Pausata et al. [2016], along with a more comprehensive discussion of the model's performances.

3 Results

This section presents the impacts of changes in Saharan vegetation and dust concentration on precipitation and atmospheric dynamics over West Africa in each sensitivity experiment relative to the MH reference simulation (CTL). The responses in the radiative and energy

variables are then analyzed. Unless otherwise specified, the significance of the changes is estimated via a two-tailed Student's t-test at the 95% confidence level.

3.1 Precipitation and Dynamics

In the CTL simulation (Figure 2a), the climatological WAM precipitation is consistent with the "classical" pattern observed in the PI and historical periods [Nicholson, 2013]. The peak precipitation reaches over 16 mm/day on the western coastline around 10^{o} N, and approximately 10 mm/day in the interior, slightly in excess of present-day observations (not shown), but in agreement with the most CMIP5 models [Harrison et al., 2014]. The northernmost extent of the monsoon is just above 16°N, 2° latitude further north than a PI simulation performed using the same model (see Figure S6 in Pausata et al. [2016]). The main change in the precipitation pattern in the GSRD experiment is a dramatic increase of precipitation over the whole North African subcontinent, with significant anomalies spanning 10^{o}N to 25^{o}N and extending to the Mediterranean coast in the western sector (Figures 2b, c). The response in the GSPD experiment (Figures 2d, e) is qualitatively similar to the GSRD experiment, though slightly weaker in intensity and extension, suggesting that the dust reduction tends to enhance the vegetation forcing (see the GSRD-GSPD difference in Figure 2h). In the Green Sahara experiments, the location of the precipitation maximum is around 15^{o}N (Figure 2b, d), consistently with the proxy-based estimation by Hély et al. [2014]. The simulated yearly precipitation anomalies exceed 700 mm around the peak (10^{o}-20^{o}N), and reach 300 mm in the Sahara region (20^{o}-30^{o}N). Skinner and Poulsen [2016] find similar precipitation anomalies extending into the late monsoonal season, pointing out the role of extratropical troughs advecting tropical moisture toward the Sahara in the form of concentrated plumes of water vapor. These values are in line with MH precipitation

245 reconstructions based on diverse paleoclimate proxies, which estimate the difference with the
246 present day over West Africa in the range 300-500 mm [Kröpelin et al., 2008; Harrison et al.,
247 2014; Tierney et al., 2017]. On the other hand, the reduction of dust alone in the PSRD
248 experiment leads to reduced precipitation over the Sahelian belt relative to the CTL case
249 (Figures 2f, g).
250
251 The wind pattern at 925 hPa in the CTL simulation is dominated by the southwesterly moist
252 monsoonal flow from the Tropical Atlantic, the northeasterly Harmattan dry wind, and the
253 cyclonic gyre associated with the Saharan Heat Low (SHL, [Lavaysse et al., 2009]), located
254 around [10°W-10°E, 20°-30°N] (Figure 3a). In the GSRD experiment (Figure 3b), the mean
255 wind pattern displays a general northward shift, relative to the MH CTL simulation, resulting
256 in an intensification of the monsoonal flow and a weakening of the Harmattan wind and the
257 SHL (-2.1 K at the peak). The latter migrates 3.2° to the north (Figure 3c), coherently with
258 the precipitation response shown in Figures 2b, c. In comparison to the GSRD experiment,
259 the GSPD experiment shows a similar response in the wind field (Figure 3h), with a slightly
260 stronger SHL (+0.9 K at the peak), displaced 0.7° to the south (Figure 3d, e). The negative
261 precipitation response in the Sahel simulated in the PSRD experiment (Figures 2f, g) is
262 instead associated with a weakening of the monsoonal flow and a deeper southward
263 penetration of the Harmattan in the eastern Sahel, accompanied by a 0.7 ° southward
264 migration of the SHL (Figures 3f, g).
265
266 In the CTL simulation, the mid-tropospheric (700 hPa) wind field appears similar, in its main
267 features, to the circulation pattern characterizing the present-day WAM (Figure 4a). The
268 African Easterly Jet (AEJ) axis is located around 16°N, and the anticyclonic gyre of the
269 Saharan high contrasts the SHL in the lower troposphere [Chen, 2005]. The GSRD

experiment shows a dramatic reorganization of the circulation, with a significant 6.5° northward shift and 2.7 m/s weakening of the AEJ, and the installation of a westerly flow around 10-15°N. This results in a large-scale cyclonic gyre over West Africa around 15°N, and a substantial weakening of the Saharan high (Figures 4b, c). The wind field response in the GSPD experiment shows a similar structure in comparison with the GSRD experiment, but in this case the Saharan high is slightly stronger and the AEJ is slightly weaker and displaced 1.2° to the south (Figures 4d, e, h). In present-day atmospheric dynamics, the AEJ is maintained by the soil moisture gradient at the surface and the two meridional circulations forced by the dry convection of the SHL to the north and the moist convection associated with the intertropical convergence zone (ITCZ) to the south [Thorncroft and Blackburn 1999; Wu et al. 2009]. Therefore, the weakening and northward shift of the jet in the Green Sahara scenario is the expected response to the vanished surface soil moisture gradient and the substantial reduction of the SHL-associated circulation. In the PSRD experiment, the only significant change is a 1.5° southward shift of the AEJ compared to the CTL (Figures 4f, g). Very similar response patterns are observed at 500 hPa (Figure S4), pointing to the emergence of an intense westerly flow around 10°N from low levels up to the mid-troposphere, and a remarkable limitation in the southward extension of the Saharan high in the GSRD and GSPD experiments.

The upper tropospheric circulation at 200 hPa is dominated by the Tropical Easterly Jet (TEJ) axis between 0 and 15°N over Africa, the subtropical jet from the Mediterranean Sea to mid-latitudes in western Asia, and the subpolar jet at mid-latitudes over the North Atlantic (Figure 5a). The GSRD and GSPD experiments (Figures 5b-e) show a general intensification of the zonal circulation in the upper troposphere, characterized by a northward shift of the subtropical jet and the emergence of an easterly jet streak around 15°N over West Africa. The

responses in GSRD and GSPD are not significantly different (Figures 5c, e, h). The response of the zonal circulation in the upper troposphere to the greening of the Sahara is interpreted as the upper branch of an anomalous Walker-like circulation (Figure S5), generated by the widespread intensification of deep convection, and connected with the strengthened westerly flow in the lower troposphere (see Figures 3c ,e). In the PSRD experiment, the zonal circulation is weakened and shifted slightly southward (Figures 5f, g).

The dramatic reorganization of the regional circulation in the GSRD experiment is also revealed by the meridional overturning circulation averaged over West Africa [10^{o}W, 10^{o}E] (Figure 6). The CTL experiment simulates a circulation pattern resembling the large scale dynamics associated with the present-day WAM (Figure 6a): (i) the southern hemisphere Hadley cell, (ii) the southerly monsoonal flow in the lower troposphere reaching the Sahel, (iii) the deep convection associated with the ITCZ, (iv) the dry shallow convection over the Sahara associated with the SHL, contrasting with the subsidence associated with the Saharan high in the mid-troposphere (500-600 hPa) [Nicholson, 2013]. In the GSRD and GSPD experiments, the change in surface conditions over the Sahara leads to an extension of the deep convection up to 30-35^{o}N, which cancels the mid-tropospheric divergence associated with the SHL shallow convection contrasting the Saharan high subsidence (Figures 6b, d). The reduction in dust concentration amplifies the response to the land cover change, inducing stronger anomalies in deep convection over the Sahel and the Sahara desert (Figures 6c, e, h). The PSRD experiment does not show any substantial systematic changes in the atmospheric meridional overturning circulation compared to the CTL experiment (Figure 6f, g).

The analysis discussed above shows that a greening of the Sahara has a dramatic impact on West African precipitation, introducing unusual features in the monsoon-related regional

circulation. Summarizing, rainfall intensifies over the Sahara and extends all the way up to the Mediterranean coast (Figure 2), and some of the dynamical features characterizing the "classical" WAM picture are substantially altered. The monsoonal flow extends far to the north and into the mid-troposphere, weakening the AEJ and shifting it northward by 6.5^{o} (Figures 3 and 4). Moreover, the mid-tropospheric contrast between the SHL convection and the Saharan high subsidence vanishes (Figures 3 and 4). These changes appear as a general reorganization of the circulation towards a cyclonic gyre throughout the troposphere, resulting from the development of deep convection over the Sahara (Figure 6). Patricola and Cook [2007] described similar modifications to the monsoonal dynamics during the MH, by prescribing shrubland north of approximately 20° in regional climate model simulations. The present study highlights that the reduction in dust concentration, following the greening of the Sahara, amplifies the impact of land cover change. On the other hand, the effect of reduction in dust alone results in a weak decrease in the Sahelian precipitation, accompanied by small changes in the atmospheric circulation. This suggests a peculiar role of dust reduction in amplifying the anomalies when associated with land cover changes.

The changes in the WAM atmospheric dynamics are accompanied by important changes in the mechanisms driving the precipitation. A major source of synoptic-scale rainfall variability throughout present-day West Africa is associated with the African easterly waves (AEWs): westward propagating disturbances with wavelengths of approximately 3000 km and periods below 5-6 days [Diedhiou et al., 1998]. A longer-period regime of 6-9 day waves has also been identified in the region [Diedhiou et al., 1998; 1999], but these typically display a weaker association with precipitation [Gu et al., 2004]. The AEWs are particularly important over the Sahel, where they modulate rainfall through the initiation and organization of mesoscale convective systems (MCSs) and squall lines during the monsoonal season [Skinner

345 and Diffenbaugh, 2013]. AEW activity is detected in each experiment by computing the
346 variance of the daily meridional wind at 700 hPa, after the application of a 2.5-5 day
347 bandpass filter. As in Diedhiou et al. [1998, 1999] and Gu et al. [2004], "wavy" days are
348 defined here as the days where the filtered southerly wind is at maximum and exceeds 0.5
349 m/s at a reference point. Such point is chosen to be representative of the main track of wave
350 activity as defined by the filtered meridional wind in the different simulations. For the CTL
351 and PSRD cases, the location [15°N, 0°E] is selected, similarly to studies analyzing the
352 present-day monsoon (e.g. Diedhiou et al., [1999]). For the GSPD and GSRD simulations,
353 the location [20°N, 0°E] is selected, reflecting the significant northward shift of the
354 monsoonal circulation. It is noted that the results are relatively insensitive to small meridional
355 shifts in the reference point (not shown, see also Gu et al., [2004]). The precipitation is then
356 averaged over the selected days and the JJAS climatology for each experiment is subtracted,
357 in order to calculate the precipitation anomalies associated with wavy days in mm/day. As a
358 caveat, it is noted that this methodology implicitly assumes that all the precipitation occurring
359 during a wavy day can be ascribed to MCSs associated to AEWs.
360
361 The CTL simulation displays a band of wave activity that originates west of the Ethiopian
362 highlands and maximizes over western Sahel, propagating across the Tropical Atlantic Ocean
363 (Figure 7a). This is similar to what seen in reanalysis data, albeit with larger variance values
364 (see Figure 3 in Skinner and Diffenbaugh [2013]). Both the GSRD and GSPD experiments
365 (Figures 7b-e) show a northward shift and a marked weakening of the meridional wind
366 variance in the region affected by the AEW activity. The difference between GSRD and
367 GSPD indicates that the dust reduction favors a further weakening of the AEW activity in the
368 presence of a vegetated Sahara (Figure 7h). Conversely, the PSRD experiment presents a
369 weakened AEW pattern relative to the CTL simulation (Figures 7e, f).

Since the definition of a wavy day focuses on meridional wind maxima, their frequency is similar across all simulations, ranging from 25.5% in the CTL simulation to 24.0% in the PSRD case. However, the intensity of these AEW episodes shows a broader spread, with the CTL simulation displaying a mean filtered meridional wind velocity of 2.6 m/s compared to the 2.3 m/s of the GSPD case and the 2.1 m/s of the GSRD case. A one-sided two-sampled Kolmogorov-Smirnov test confirms that the cumulative distribution function of the AEW intensity for the GSPD case is larger than that of the CTL at the 95% confidence level, indicating a shift of the distribution towards lower values.

The significant differences in the filtered meridional wind variance and AEW intensity result in equally large changes in the precipitation associated with the AEWs. The precipitation on wavy days is characterized by a multipolar anomaly pattern, clearly showing the signature of a propagating wave (Figure 8). The peak precipitation anomalies driven by the AEW-associated MCSs are not co-located with the reference points at which the waves are identified. Rather, the peaks tend to occur to the west or south-west of the reference points, in close agreement with previous studies (e.g., Diedhiou et al. [1999] and Gu et al. [2004]). The peak average precipitation anomaly in the CTL simulation is 4.7 mm/day (Figure 8a), and wavy days account for 41.5% of the total seasonal precipitation at that location (Figure 8b). The GSPD and GSRD simulations display a clear northward shift of the dipole, with a sizable reduction of the average peak precipitation anomalies on wavy days to 1.6 and 2.3 mm/day, respectively (Figures 8c, e). These correspond to 36.5% and 33.3% of the total precipitation (Figures 8d, f), respectively. The dust reduction alone leads to slight changes in this pattern, with a 4.1 mm/day peak anomaly, representing 39.2% of the total precipitation.

The decreased importance of AEWs under Green Sahara conditions indicates a shift towards variability on time scales longer than the synoptic one. This is confirmed by a spectral analysis of precipitation and meridional wind at 700 hPa over [5°-16°N, 10°W-10°E] for the CTL and PSRD simulations and [5°-28°N, 10°W-10°E] for the GSRD and GSPD simulations. The different domains, as for the wavy day calculation, reflect the northward shift of the monsoon under a Green Sahara. The northern limits are chosen to roughly match the monsoon's northernmost extent, calculated following the methodology of Pausata et al. [2016]. The CTL and PSRD meridional wind spectra display a clear peak around the AEW periodicity (2-5 days), while in the two Green Sahara scenarios the power in this band is weaker, and the spectra increase almost monotonically with period (Figure 9b). The precipitation spectra (Figure 9a) reflect this difference. In the CTL and PSRD simulations there is again a clear peak matching the AEW periodicity and highlighting the waves' dominant role in driving precipitation. In the two Green Sahara scenarios, the spectra show a roughly monotonic increase with period, suggesting that the 2-5 day band only accounts for a modest fraction of the total precipitation. . Furthermore, while longer waves in the 6-9 day band grow in importance under a green Sahara, they do not play the same role as the 2-5 day band in the desert Sahara scenarios (Figure 9). The Green Sahara simulations display a higher spectral power than the desert Sahara in both meridional wind and precipitation beyond ~6 days, but there is no clear peak to suggest that a specific dynamical mechanism is acting to enhance the precipitation over this frequency range.

Summarizing, the Green Sahara scenario is characterized by a widespread increase in precipitation, accompanied by a significant reduction in the 3-5 day AEW activity and in their ability to drive precipitation. The precipitation and meridional wind spectra show a shift towards longer periods and do not display any prominent peaks. This is somewhat surprising,

because a sizable fraction of the present-day monsoonal precipitation is ascribed to the convection triggered by AEWs [Skinner and Diffenbaugh, 2013]. Hence, a more active AEW regime might be expected under an intensified MH monsoon, due to the increased latent heat and convection associated with the increased precipitation. This apparent contradiction can be reconciled by considering the role of the AEJ in triggering and strengthening the AEWs, through barotropic-baroclinic instabilities [Thorncroft and Hoskins, 1994]. Wu et al. [2012] found that synoptic disturbances are more likely where the zonal flow is stronger and that the more unstable waves are likely to be closer to the zonal flow maximum, i.e., closer to an intense AEJ core. It is therefore argued that, in the Green Sahara scenarios, the radical modification of the AEJ dynamics dominates the thermodynamic changes; the sizable northward migration (+6.5^{o}) and weakening (-2.7 m/s) being more effective in shifting and suppressing the wave activity than the latent heat and convection increase in enhancing it. Finally, it is highlighted that the dust reduction induces opposite responses in the atmospheric dynamics, depending on the land cover of the Sahara: it leads to more or less favorable conditions for precipitation, when associated with a vegetated or desert surface, respectively.

3.2 Energy budget

The rainfall and atmospheric circulation patterns simulated in the sensitivity experiments are closely linked to the changes in surface conditions and radiative properties of the atmosphere, which in turn affect the energetics and dynamics of the WAM. This section elucidates the links between energetics, precipitation and dynamics in the sensitivity experiments, through the analysis of the atmospheric radiative and heat fluxes, and moist static energy (MSE) content.

445 The greening of the Sahara (GSPD simulation) lowers the surface albedo over a vast portion
446 of North Africa (see Table 1), leading to an increase in the net flux of the clear-sky
447 downward SW radiation at the top of the atmosphere (TOA) (Figure 10c). The downward
448 SW flux anomaly is almost uniform and limited to the area where the surface albedo is
449 lowered. The reduction in dust concentration, when the Sahara is deserted (PSRD
450 simulation), leads to an upward SW flux anomaly at the TOA, in which the fingerprint of the
451 dust reduction pattern is evident (Figure 10e). The upward SW flux is due to the increase in
452 the planetary albedo produced by the removal of airborne dust over a bright surface. On the
453 contrary, the removal of airborne dust when the Sahara is vegetated (GSRD simulation)
454 further reduces the planetary albedo of a dark surface, enhancing the downward flux anomaly
455 of SW radiation simulated in the GSPD experiment (Figure 10a), although the effect is quite
456 weak (Figure 10g).
457
458 At the surface, the effect of greening the Sahara (GSPD simulation) is similar to the TOA,
459 resulting in a positive anomaly of the downward SW radiation, limited to the area where the
460 surface albedo is reduced (Figure 10d). A widespread increase in the downward SW radiation
461 at the surface is also simulated in the PSRD experiment (Figure 10f), in which the removal of
462 airborne dust reduces the absorption of the solar radiation, especially at latitudes around
463 15^{o}N, where dust concentration is maximum (see Figure 1). By reducing the absorption of
464 solar radiation, the removal of airborne dust over the Green Sahara (GSRD simulation)
465 enhances the positive anomaly in the downward SW radiation due to the lower surface albedo
466 (Figure 10b, h).
467
468 In the Green Sahara experiments, the SW radiative forcing simulated at the surface over the
469 Sahel and Sahara is accompanied by a negative (i.e. upward) anomaly in the sensible heat

(SH) flux, which reverts to positive (i.e. downward) between 10°N and 20°N due to the cooling effect of the precipitation anomalies (Figures 11a, c; cf. Figure 2). The additional SW radiative forcing in the GSRD simulation, associated with the dust reduction, limits the upward SH flux in the eastern Sahel (Figures 11a, g). In the PSRD simulation, the upward SH flux anomaly is widespread, peaking between 10°N and 20°N, where the SW radiative forcing is maximum (Figure 11e; cf. Figure 10f). The latent heat (LH) flux at the surface shows significant negative (i.e. upward) anomalies in the Green Sahara scenarios (Figures 11b, d). The release of LH into the atmosphere is associated with enhanced evaporation over the vegetated surface, induced by the SW radiative forcing. The LH response is shaped by the precipitation anomalies, further enhancing evaporation (Figures 11b, d; cf. Figure 2). The reduction in dust concentration over the Green Sahara increases SW radiative forcing and precipitation at the surface, strengthening the LH release into the atmosphere (Figure 11h). Reduction in dust concentration alone (PSRD simulation) results in LH release over the vegetated Sahel (south of 15°N), induced by the SW radiative forcing, while the decreased precipitation leads to negative anomalies in the LH flux north of 15°N (Figure 11f).

The combination of the LH and SH fluxes results in an intense upward heat flux over the Sahara in the Green Sahara experiments, and a weaker upward flux peaking over the Sahel in the PSRD experiment (Figure S6). The heat flux then triggers moist convection, whose modifications are diagnosed in the sensitivity experiments through the MSE content of the atmosphere. This is defined as the sum of geopotential, enthalpy and latent heat:

$$MSE = gz + C_p T + Lq,$$

where g is the gravitational acceleration, z the geopotential height, C_p the specific heat of dry air at constant pressure, T temperature, L the latent heat of evaporation, and q the specific humidity. The MSE is a direct indicator of the monsoonal precipitation, because the

transformation of enthalpy and latent energy available in the lower troposphere into geopotential energy aloft is the main signal of convection [Fontaine and Philippon, 2000]. In the GSRD simulation, the meridional profile of the MSE atmospheric content shows an intense positive anomaly dominating the entire troposphere from 15°N to 35°N (Figure 12a). Close to the surface, at 1000 hPa, the MSE peak moves 6° northward (from 14°N in CTL to 20°N; Figure S7), accompanied by an increase in the meridional difference between the peak and the Guinea Coast (+1.7 kJ/kg; Figure S7). The GSPD simulation shows a similar pattern, characterized by weaker anomalies (Figures 12 b, d): a +5° migration of the MSE peak and a 1.2 kJ/kg increase in the meridional difference with the Guinea Coast (Figure S7). These modifications elucidate the precipitation response in the Green Sahara experiments: the meridional migration and intensification of the peak MSE favor the northward penetration of the precipitation belt, and the MSE excess in the lower-middle troposphere triggers deep convection over the Sahara. In the PSRD simulation (Figure 12c), the MSE content shows a negative anomaly in the middle-upper troposphere, and a weakening of the maximum close to the surface (-0.7 kJ/kg at 1000 hPa; Figure S7), resulting in a weaker monsoonal circulation.

4 Discussion and conclusions

The objective of this study is to improve the understanding of the changes in the West African monsoon dynamics and precipitation patterns during the mid-Holocene, when large part of North Africa was characterized by a mesic environment and the Sahara desert was extensively covered by vegetation. A set of idealized sensitivity experiments, performed with the EC-Earth climate model, has been used to understand the changes in atmospheric circulation that characterized that period. In these simulations, vegetation cover over the

519 Sahara and a reduction in atmospheric mineral dust concentrations are imposed together and
520 in turn.
521
522 By using these set of simulations, Pausata et al. [2016] showed that the vegetation cover over
523 the Sahara is the primary driver of a radical alteration of the West African monsoon during
524 the mid-Holocene, with the associated dust reduction further strengthening precipitation
525 anomalies inland. The precipitation simulated in their "Green Sahara and reduced dust"
526 experiment is indeed quantitatively consistent with estimations of the mid-Holocene
527 precipitation based on paleoclimate proxy data [Tierney et al., 2017]. This study further
528 extends the analysis performed by Pausata et al. [2016], to improve the understanding of the
529 changes in the monsoonal dynamics accompanying the precipitation anomalies. The
530 modifications of the radiative balance at the surface and the TOA are also discussed, along
531 with the consequent response of the energetics of the monsoonal system.
532
533 When a vegetation cover is prescribed over the Sahara (GSPD), a dramatic response in the
534 West African monsoon is simulated. The lowering of the surface albedo induces an intense
535 positive radiative forcing at the TOA and at the surface over the Sahara, leading to a release
536 of sensible and latent heat into the atmosphere. The heat flux anomaly triggers moist
537 convection over this region, driving a northward expansion of the monsoonal precipitation
538 belt, which extends up to the Mediterranean coast. A substantial modification of the regional
539 circulation is also simulated, with critical alterations in some of the "classical" dynamical
540 features of the West African monsoon, such as the Saharan heat low, the African easterly jet,
541 and the African easterly wave regime. In particular, a weakening of the African easterly wave
542 activity is associated with a decrease in wave-related precipitation, suggesting a reduction of
543 the African easterly waves' role in triggering and organizing mesoscale convective systems.

These changes follow a general reorganization of the circulation towards a cyclonic gyre throughout the troposphere. This analysis suggests that a vegetated Sahara may radically change the regional circulation pattern over West Africa.

On the opposite, dust reduction alone (PSRD) leads to a slight weakening in the monsoonal circulation and precipitation rates. This weakening is associated with a positive surface radiative forcing in the Sahel and a radiative cooling in the middle-upper troposphere over the Sahara, resulting in a reduction of the meridional energy gradient over West Africa, which prevent monsoonal precipitation to penetrate inland.

The effect of dust removal on the radiative balance of the atmosphere depends on the radiative properties of the airborne dust in association with the underlying land cover. Indeed, in PI conditions dust reduction increases the planetary albedo above the Sahara desert, cooling the middle-upper troposphere, and induces a positive radiative forcing at the surface, peaking in the vegetated Sahel. On the contrary, when a vegetated surface is prescribed from the Sahel to the Sahara, dust reduction lowers the planetary albedo, warming the middle-upper troposphere, and induces a positive radiative forcing at the surface, peaking in the Sahel-Sahara transition zone where PI dust concentration is maximum.

The radical modification of the atmospheric circulation over North Africa discussed in this study is likely to have trigged a chain of global-scale changes during the mid-Holocene. For example, Muschitiello et al. [2015], using the same model as in this study, show that the desertification of the Sahara at the end of the African humid period led to a reduction in the atmospheric and oceanic poleward heat transport from tropical to high northern latitudes. The reduction in the poleward heat transport weakened the mid-latitude westerlies, resulting in

569 more negative Arctic Oscillation-like conditions and a consequent cooling over the Arctic
570 and North Atlantic regions. Results presented in this paper show that the greening of the
571 Sahara triggers a strong reduction in African easterly wave activity, which is known to be
572 related with the formation of tropical cyclones in the Atlantic Ocean [Price et al., 2015].
573 Therefore, the decreased AEW activity may induce a reduction in tropical storms developing
574 in the North Atlantic. On the other hand, the reduction in the Saharan dust emission and
575 transport across the tropical Atlantic is favorable to the development of tropical cyclones in
576 the basin, through the radiative warming of the ocean surface [Evan et al., 2006], indicating
577 possible competing effects of the vegetation-dust changes in the Sahara on the Atlantic
578 hurricane season. Furthermore, reducing African easterly waves may initially lead to fewer
579 tropical cyclones but, because of that, the ocean would warm, compensating for the reduced
580 wave activity (assuming no other changes in the thermodynamic structure of the atmosphere).
581 Therefore, the combination of Sahara greening and reduced dust emission during the mid-
582 Holocene may have led to an increased number of tropical cyclones in the Atlantic. By
583 analyzing the same set of simulations used in this study, Pausata et al. [2017a] show indeed
584 an increase in the tropical cyclone activity in both the hemispheres and particularly over the
585 Caribbean basin and the east coast of North America. This hypothesis cannot be tested with
586 current paleotempestology archives that are geographically and temporally patchy, and hence
587 unable to provide a complete view of the Holocene storm activity. However, a proxy-data
588 reconstruction from Puerto Rico suggests a positive correlation between West African
589 monsoon strength and tropical cyclone intensity over the last 5500 years [Donnelly &
590 Woodruff, 2008]. In particular, the period between 2500 and 1000 years BP was the most
591 active tropical storm interval in Puerto Rico and was characterized by a stronger WAM and a
592 reduced Saharan dust flux relative to the following millennium [Mulitza et al., 2010]. In
593 addition, Williams et al. [2016] emphasized the relationship between reduced dust loading

during the early and mid-Holocene and the northward expansion of the ITCZ, which in turn can intensify tropical storm activity in the western North Atlantic [van Hengstum et al., 2016]. Pausata et al. [2017b] also show reduced El Niño-Southern Oscillation (ENSO) variability and La Niña-like conditions in winter in a Green Sahara scenario, compared to pre-industrial and the standard CMIP/PMIP mid-Holocene scenarios. These changes in ENSO mean state and variability are in general favorable to tropical storm activity in the North Atlantic basin [Chiacchio et al., 2017]. Further efforts both from the modelling and the proxy community are necessary to better understand the remote teleconnections associated to the West African monsoon variability.

The findings of this study are also useful also in a future perspective, at regional and global scales. Indeed, the possible positive trend in Sahelian precipitation projected for the 21st century [Biasutti, 2013] may be accompanied and amplified by land cover and dust reduction feedbacks, which in turn may impact climate in remote regions.

Acknowledgements

M. G. has been supported by the LABEX project, funded by Agence Nationale de la Recherche (French National Research Agency, grant ANR-10-LABX-18-01). G. M. has been supported by the MILEX project, funded by the Swedish Research Council (Vetenskapsrådet grant 2012-40395-98427-17) and a grant from the Department of Meteorology of Stockholm University. Q.Z. acknowledges funding from Swedish Research Council VR for the Swedish-French project “Greenland in a warming Arctic”. F.S.R.P. acknowledges funding from the Swedish Research Council (FORMAS) as part of the Joint Programming Initiative on Climate and the Belmont Forum for the project “Palaeo-constraints on Monsoon Evolution

and Dynamics (PACMEDY)" (grant FR-2016/0001). The simulations with EC-Earth were performed on supercomputer provided by the Swedish National Infrastructure for Computing (SNIC) at NSC and Cray XC30 HPC systems at ECMWF. The authors thank three anonymous reviewers for their constructive comments, which led to a substantial improvement of the manuscript.

625 **References**

626

627 Albani, S., N. M. Mahowald, A. T. Perry, R. A. Scanza, C. S. Zender, N. G. Heavens, V.
628 Maggi, J. F. Kok, and B. L. Otto-Bliesner (2014), Improved dust representation in the
629 Community Atmosphere Model, J. Adv. Model. Earth Syst., 6, 541–570,
630 doi:10.1002/2013MS000279.
631 Biasutti, M. (2013), Forced Sahel rainfall trends in the CMIP5 archive, J. Geophys. Res.
632 Atmos., 118, 1613–1623, doi:10.1002/jgrd.50206.
633 Biasutti, M., A. H. Sobel, and S. J. Camargo (2009), The Role of the Sahara Low in
634 Summertime Sahel Rainfall Variability and Change in the CMIP3 Models, J. Clim., 22,
635 5755–5771, doi:10.1175/2009JCLI2969.1.
636 Braconnot, P., S.P. Harrison, B. Otto-Bliesner, A. Abe-Ouchi, J. Jungclaus, and J.Y.
637 Peterschmitt (2011), The Paleoclimate Modeling Intercomparison Project contribution to
638 CMIP5, CLIVAR Exchanges No. 56, 16, 15-19.
639 Chen, T. C. (2005), Maintenance of the midtropospheric North African summer circulation;
640 Saharan high and African easterly jet, J. Clim., 18, 2943–2962, doi:10.1175/JCLI3446.1.
641 Chiacchio, M., F. S. R. Pausata, G. Messori, A. Hannachi, M. Chin, T. Önskog, A. M. L.
642 Ekman, and L. Barrie (2017), On the links between meteorological variables, aerosols,
643 and tropical cyclone frequency in individual ocean basins, J. Geophys. Res. Atmos.,
644 122, 802–822, doi:10.1002/2015JD024593.
645 Claussen, M. and V. Gayler (1997), The greening of the Sahara during the mid-Holocene:
646 results of an interactive atmosphere-biome model, Global Ecology and Biogeography
647 Letters, 6, 369-377.
648 deMenocal, P. B., J. Ortiz, T. Guilderson, J. Adkins, M. Sarnthein, L. Baker, and M.
649 Yarusinsky (2000), Abrupt onset and termination of the African Humid Period: Rapid

650 climate responses to gradual insolation forcing, Quat. Sci. Rev., 19, 347–361,
651 doi:10.1016/S0277-3791(99)00081-5.
652 Diedhiou A., S. Janicot, A. Viltard, P. de Felice, and H. Laurent (1998), Evidence of two
653 regimes of easterly waves over West Africa and the tropical Atlantic. Geophys. Res.
654 Let., 25, 2805-2808.
655 Diedhiou A., S. Janicot, A. Viltard, P. De Felice, and H. Laurent (1999), Easterly waves
656 regimes and associated convection over West Africa and the tropical Atlantic: results
657 from the NCEP/NCAR and ECMWF reanalyses. Clim. Dyn.,15, 795-822.
658 Donnelly, J. P. and J. D. Woodruff (2007), Intense hurricane activity over the past 5,000
659 years controlled by El Niño and the West African monsoon, Nature, 447, 465-468.
660 ECMWF (2010), ECMWF Newsletter No. 126, Winter 2010/11
661 (http://www.ecmwf.int/sites/default/files/elibrary/2010/14597-newsletter-no126-winter-
662 201011.pdf).
663 Egerer, S., M. Claussen, C. Reick, and T. Stanelle (2016), The link between marine sediment
664 records and changes in Holocene Saharan landscape: simulating the dust cycle, Clim.
665 Past, 12, 1009-1027, doi:10.5194/cp-12-1009-2016.
666 Evan, A. T., J. Dunion, J. A. Foley, A. K. Heidinger, and C. S. Velden (2006), New evidence
667 for a relationship between Atlantic tropical cyclone activity and African dust outbreaks,
668 Geophys. Res. Lett., 33, L19813, doi:10.1029/2006GL026408.
669 Evan A.T., C. Flamant, M. Gaetani, and F. Guichard (2016), The Past, Present and Future of
670 African Dust. Nature, 531, 493-495, doi:10.1038/nature17149.
671 Fontaine, B., and N. Philippon (2000), Seasonal Evolution of Boundary Layer Heat Content
672 in the West African Monsoon From the NCEP/NCAR, Int. J. Climatol., 20, 1777–1790.
673 Gaetani, M., C. Flamant, S. Bastin, S. Janicot, C. Lavaysse, F. Hourdin, P. Braconnot, S.
674 Bony (2016), West African monsoon dynamics and precipitation: the competition

675 between global SST warming and CO2 increase in CMIP5 idealized simulations, Clim.
676 Dyn., doi:10.1007/s00382-016-3146-z.
677 Gasse, F. (2000), Hydrological changes in the African tropics since the Last Glacial
678 Maximum. Quat. Sci. Rev., 19, 189–211.
679 Giannini, A. (2010), Mechanisms of Climate Change in the Semiarid African Sahel: The
680 Local View, J. Clim., 23, 743–756, doi:10.1175/2009JCLI3123.1.
681 Ginoux, P., J. M. Prospero, T. E. Gill, N. C. Hsu, and M. Zhao (2012), Global-scale
682 attribution of anthropogenic and natural dust sources and their emission rates based on
683 MODIS Deep Blue aerosol products, Rev. Geophys., 50, 1–36,
684 doi:10.1029/2012RG000388.
685 Gu, G., R. F. Adler, G. J. Huffman, and S. Curtis (2004), African easterly waves and their
686 association with precipitation, J. Geophys. Res., 109, D04101,
687 doi:10.1029/2003JD003967.
688 Harrison, S. P., P. J. Bartlein, S. Brewer, I. C. Prentice, M. Boyd, I. Hessler, K. Holmgren, K.
689 Izumi, and K. Willis (2014), Climate model benchmarking with glacial and mid-
690 Holocene climates, Clim. Dyn., 43, 671–688, doi:10.1007/s00382-013-1922-6.
691 Harrison, S.P., P.J. Bartlein, K. Izumi, G. Li, J. Annan, J. Hargreaves, P. Braconnot, M.
692 Kageyama (2015), Evaluation of CMIP5 palaeo-simulations to improve climate
693 projections, Nat. Clim. Change, 5, 735–743, doi:http://dx.doi.org/10.1038/
694 nclimate2649.
695 Hazeleger, W., et al. (2010), EC-Earth: A Seamless Earth-System Prediction Approach in
696 Action, Bull. Am. Meteorol. Soc., 91, 1357–1363, doi:10.1175/2010BAMS2877.1.
697 Hély, C., A.-M. Lézine, and APD contributors (2014), Holocene changes in African
698 vegetation: tradeoff between climate and water availability, Clim. Past, 10, 681–686,
699 doi:10.5194/cp-10-681-2014.

700 Holmes, J. A., (2008), How the Sahara became dry. Science 320, 752–753,
701 doi:10.1126/science.1158105.
702 IFAD (2013), Rainfed Food Crops in West and Central Africa : Rainfed Food Crops in West
703 and Central Africa, A Savoir, July 2013.
704 Kröpelin, S., D. Verschuren, A.-M. Lézine, H. Eggermont, C. Cocquyt, P. Francus, J.-P.
705 Cazet, M. Fagot, B. Rumes, J.M. Russell, F.Darius, D.J. Conley, M. Schuster, H. von
706 Suchodoletz, D.R. Engstrom (2008), Climate-driven ecosystem succession in the
707 Sahara: the past 6000 years, Science, 320, 765-768,
708 http://dx.doi.org/10.1126/science.1154913.
709 Lavaysse, C., C. Flamant, S. Janicot, D. J. Parker, J. P. Lafore, B. Sultan, and J. Pelon (2009),
710 Seasonal evolution of the West African heat low : a climatological perspective, Clim.
711 Dyn., 33, 313–330.
712 Levis, S., Bonan G. B., and Bonfils C. (2004), Soil feedback drives the mid-Holocene North
713 African monsoon northward in fully coupled CCSM2 simulations with a dynamic
714 vegetation model, Clim. Dyn., 23, 791-802, doi:10.1007/s00382-004-0477-y.
715 Lézine, A.-M., C. Hély, C. Grenier, P. Braconnot, and G. Krinner (2011), Sahara and Sahel
716 vulnerability to climate changes, lessons from Holocene hydrological data, Quat. Sci.
717 Rev., 30, 3001–3012, doi:10.1016/j.quascirev.2011.07.006.
718 Madec, G. (2008), NEMO ocean engine, Note du Pole de modlisation, Institut Pierre-Simon
719 Laplace (IPSL), Paris, France, No. 27, ISSN No. 1288-1618
720 (http://www.nemoocean.eu/About-NEMO/Reference-manuals).
721 McGee, D., P. B. deMenocal, G. Winckler, J. B. W. Stuut, and L. I. Bradtmiller (2013), The
722 magnitude, timing and abruptness of changes in North African dust deposition over the
723 last 20,000yr, Earth Planet. Sci. Lett., 371-372, 163–176,
724 doi:10.1016/j.epsl.2013.03.054.

725 Mulitza, S., D. Heslop, D. Pittauerova, H.W. Fischer, I. Meyer, J.-B. Stuut, M. Zabel, G.
726 Mollenhauer, J.A. Collins, H. Kuhnert and M. Schulz (2010), Increase in African dust
727 flux at the onset of commercial agriculture in the Sahel region, Nature, 466, 226-228.
728 Muschitiello, F., Q. Zhang, H. S. Sundqvist, F. J. Davies, and H. Renssen (2015), Arctic
729 climate response to the termination of the African Humid Period, Quaternary Science
730 Reviews, 125, 91-97, doi:10.1016/j.quascirev.2015.08.012.
731 Nicholson, S. E. (2013), The West African Sahel: A Review of Recent Studies on the
732 Rainfall Regime and Its Interannual Variability, ISRN Meteorol., 2013, 453521,
733 doi:10.1155/2013/453521.
734 Patricola, C. M., and K. H. Cook (2007), Dynamics of the West African Monsoon under Mid-
735 Holocene Precessional Forcing: Regional Climate Model Simulations, J. Clim., 20, 694-
736 716, doi:10.1175/JCLI4013.1.
737 Patricola, C. M., and K. H. Cook (2008), Atmosphere/vegetation feedbacks: A mechanism
738 for abrupt climate change over northern Africa, J. Geophys. Res., 113, D18102,
739 doi:10.1029/2007JD009608.
740 Pausata, F. S. R., K. A. Emanuel, M. Chiacchio, G. T. Diro, Q. Zhang, L. Sushama, J. C.
741 Stager, and J. P. Donnelly (2017a), Tropical cyclone activity enhanced by Sahara
742 greening and reduced dust emissions during the African Humid Period. Proc. Natl.
743 Acad. Sci., doi:10.1073/pnas.1619111114.
744 Pausata, F. S. R., G. Messori, and Q. Zhang (2016), Impacts of dust reduction on the
745 northward expansion of the African monsoon during the Green Sahara period, Earth
746 Planet. Sci. Lett., 434, 298–307, doi:10.1016/j.epsl.2015.11.049.
747 Pausata F. S. R., Q. Zhang, F. Muschitiello, Z. Lu, L. Chafik, E.M. Niedermeyer, J.C. Stager,
748 K.M. Cobb, and Z. Liu (2017b), Greening of the Sahara suppressed ENSO activity
749 during the Mid-Holocene, Nature Communications, in press.

750 Price, C., N. Reicher, and Y. Yair (2015), Do West African thunderstorms predict the
751 intensity of Atlantic hurricanes?, Geophys. Res. Lett., 42, 2457–2463,
752 doi:10.1002/2014GL062932.
753 Rachmayani, R., M. Prange, and M. Schulz (2015), North African vegetation-precipitation
754 feedback in early and mid-Holocene climate simulations with CCSM3-DGVM, Clim.
755 Past., 11, 175–185, doi:10.5194/cp-11-175-2015.
756 Rodríguez-Fonseca, B., et al. (2015), Variability and Predictability of West African
757 Droughts: A Review on the Role of Sea Surface Temperature Anomalies, J. Clim., 28,
758 4034–4060, doi:10.1175/JCLI-D-14-00130.1.
759 Roehrig, R., D. Bouniol, F. Guichard, F. D. Hourdin, and J. L. Redelsperger (2013), The
760 present and future of the west african monsoon: A process-oriented assessment of
761 CMIP5 simulations along the AMMA transect, J. Clim., 26, 6471–6505,
762 doi:10.1175/JCLI-D-12-00505.1.
763 Rowell, D. P. (2013), Simulating SST teleconnections to Africa: What is the state of the art?,
764 J. Clim., 26, 5397–5418, doi:10.1175/JCLI-D-12-00761.1.
765 Schmidt, G. A., et al. (2014), Using palaeo-climate comparisons to constrain future
766 projections in CMIP5, Clim. Past, 10, 221–250, doi:10.5194/cp-10-221-2014.
767 Shanahan, T.M., J.T. Overpeck, C.W. Wheeler, J.W. Beck, J.S. Pigati, M.R. Talbot, C. A.
768 Scholzg, J. Peckh, J. W. Kingi (2006), Paleoclimatic variations in West Africa from a
769 record of late Pleistocene and Holocene lake level stands of Lake Bosumtwi, Ghana.
770 Palaeogeography, Palaeoclimatology, Palaeoecology, 242, 287-302,
771 doi:10.1016/j.palaeo.2006.06.007
772 Skinner, C. B., and N. S. Diffenbaugh (2013), The contribution of African easterly waves to
773 monsoon precipitation in the CMIP3 ensemble, J. Geophys. Res. Atmos., 118, 3590–
774 3609, doi:10.1002/jgrd.50363.

775 Skinner, C. B., and C. J. Poulsen (2016), The role of fall season tropical plumes in enhancing
776 Saharan rainfall during the African Humid Period, Geophys. Res. Lett., 43, 349–358,
777 doi:10.1002/2015GL066318.
778 Su, H., and J. D. Neelin (2005), Dynamical mechanisms for African monsoon changes during
779 the mid-Holocene, J. Geophys. Res., 110, D19105, doi:10.1029/2005JD005806
780 Sultan, B., and M. Gaetani (2016), Agriculture inWest Africa in the Twenty-First Century:
781 Climate Change and Impacts Scenarios, and Potential for Adaptation. Front. Plant Sci.,
782 7, 1262, doi:10.3389/fpls.2016.01262.
783 Swann, A. L. S., I. Y. Fung, Y. Liu, and J. C. H. Chiang (2014), Remote Vegetation
784 Feedbacks and the Mid-Holocene Green Sahara, J. Clim., 27, 4857-4870,
785 doi:10.1175/JCLI-D-13-00690.1.
786 Taylor, K. E., R. J. Stouffer, and G. A. Meehl (2012), An overview of CMIP5 and the
787 experiment design, Bull. Am. Meteorol. Soc., 93, 485–498, doi:10.1175/BAMS-D-11-
788 00094.1.
789 Thorncroft, C. D., and M. Blackburn (1999), Maintenance of the African easterly jet, Q. J. R.
790 Meteorol. Soc., 125, 763-786, doi:10.1002/qj.49712555502.
791 Thorncroft, C. D., and B. J. Hoskins (1994), An idealized study of African easterly waves. I:
792 A linear view. Q.J.R. Meteorol. Soc., 120: 953–982. doi:10.1002/qj.49712051809.
793 Tierney, J. E., F. S. R. Pausata, and P. B. deMenocal (2017), Rainfall regimes of the Green
794 Sahara. Sci. Adv., 3: e1601503, doi:10.1126/sciadv.1601503
795 Valcke, S. (2006), OASIS3 user guide, PRISM Tech. Rep. 3, 64 pp., Partnership for Res.
796 Infrastructures in Earth System Modeling, Toulouse, France
797 (http://www.prism.enes.org/Publications/Reports/oasis3_UserGuide_T3.pdf).
798 Vancoppenolle, M., T. Fichefet, H. Goosse, S. Bouillon, G. Madec, and M. A. Morales
799 Maqueda (2008), Simulating the mass balance and salinity of Arctic and Antarctic sea

ice. 1. Model description and validation, Ocean Model., 27, 33-53, doi:10.1016/j.ocemod.2008.10.005.

van den Hurk, B., P. Viterbo, A. Beljaars, and A.K. Betts (2000), Offline validation of the ERA-40 surface scheme, ECMWF Tech. Memo. No. 295, ECMWF, Reading, UK.

van Hengstum P. J., J. P. Donnelly, P. L. Fall, M. R. Toomey, N. A. Albury, and B. Kakuk (2016), The intertropical convergence zone modulates intense hurricane strikes on the western North Atlantic margin, Sci. Rep., 6, 21728.

Williams R.H., D. McGee, C. W. Kinsley, D. A. Ridley, S. Hu, A. Fedorov, I. Tal, R. W. Murray, and P. B. deMenocal (2016), Glacial to Holocene changes in trans-Atlantic Saharan dust transport and dust-climate feedbacks, Sci. Adv., 2, e1600445, doi:10.1126/sciadv.1600445

Wu, M.-L.C., O. Reale, S.D. Schubert, M.J. Suarez, R.D. Koster, and Philip J. Pegion (2009), African Easterly Jet: Structure and Maintenance, J. Climate, 22, 4459-4480, doi:10.1175/2009JCLI2584.1.

Wu, M.-L.C., O. Reale, S.D. Schubert, M.J. Suarez, and Chris D. Thorncroft (2012), African Easterly Jet: Barotropic Instability, Waves, and Cyclogenesis, J. Climate, 25, 1489-1510, doi:10.1175/2011JCLI4241.1.

Tables

Table 1: Experimental design used in the control simulation (CTL) and the sensitivity experiments: present-day Sahara and reduced dust (PSRD); Green Sahara and reduced dust (GSRD); Green Sahara and pre-industrial dust (GSPD).

Simulation	Orbital forcing (years BP)	GHGs	Vegetation type	Albedo	LAI	Saharan dust
CTL	6k	MH	Desert	0.30	0	PI
PSRD	6k	MH	Desert	0.30	0	80% reduced
GSRD	6k	MH	Evergreen shrub	0.15	2.6	80% reduced
GSPD	6k	MH	Evergreen shrub	0.15	2.6	PI

Figures

Figure 1: (left) JJAS pre-industrial dust mixing ratio [kg/kg], prescribed in the CTL and GSPD simulations, and (right) difference between reduced dust and pre-industrial concentration. (a, b) Column integral, (c, d) vertical profile averaged in the range [15°W, 25°E], (e, f) meridional profile of the column integral.

Figure 2: JJAS precipitation [mm/day]: (left) climatological means for the CTL simulation and the sensitivity experiments, and (right) differences between the sensitivity experiments and the CTL simulation. In panel (h), the difference between the GSRD and GSPD experiments is shown. Significance at 95% confidence level is displayed.

Figure 3: JJAS wind field at 925 hPa [m/s]: (left) climatological means for the CTL simulation and the sensitivity experiments, and (right) differences between the sensitivity experiments and the CTL simulation. In panel (h), the difference between the GSRD and GSPD experiments is shown. Significance at 95% confidence level is displayed. Shadings indicate the Saharan heat low location and intensity, represented through the values of air temperature at 850 hPa [K] exceeding the 90th percentile in the domain [0-40°N, 20°W-20°E] [Lavaysse et al., 2009]. The SHL position and intensity is determined by detecting the maximum of the air temperature at 850 hPa inside the domain.

Figure 4: JJAS wind field at 700 hPa [m/s]: (left) climatological means for the CTL simulation and the sensitivity experiments, and (right) differences between the sensitivity experiments and the CTL simulation. In panel (h), the difference between the GSRD and GSPD experiments is shown. Significance at 95% confidence level is displayed. Shadings

indicate the Saharan high location and intensity, represented through the geopotential height at 700 hPa exceeding 3150 m. Red lines represent the mean positions of the African easterly jet in the CTL simulation (dashed) and the sensitivity experiments (solid). The mean axis of the African easterly jet is determined in the domain [20°W-20°E, 0°-40°N] by detecting, at each longitude, the latitudinal location of the minimum of the zonal wind at 700 hPa, and averaging along the zonal direction.

Figure 5: JJAS wind field at 200 hPa [m/s]: (left) climatological means for the CTL simulation and the sensitivity experiments, and (right) differences between the sensitivity experiments and the CTL simulation. In panel (h), the difference between the GSRD and GSPD experiments is shown. Significance at 95% confidence level is displayed.

Figure 6: JJAS meridional overturning circulation, represented through the meridional wind [m/s] and the vertical velocity [Pa/s], averaged in the range [10^{o}W, 10^{o}E]: (left) climatological means for the CTL simulation and the sensitivity experiments, and (right) differences between the sensitivity experiments and the CTL simulation. In panel (h), the difference between the GSRD and GSPD experiments is shown. Significance at 95% confidence level is displayed.

Figure 7: JJAS African easterly wave activity, represented through the variance of the meridional wind at 700 hPa filtered in the 2.5-5-day band [m^2/s^2]: (left) climatological means for the CTL simulation and the sensitivity experiments, and (right) differences between the sensitivity experiments and the CTL simulation. In panel (h), the difference between the GSRD and GSPD experiments is shown. Significance at 95% confidence level is displayed, computed by using a two-sample F test.

Figure 8: Precipitation associated with the African easterly waves detected in JJAS at locations indicated by black crosses: (left) precipitation anomalies [mm/day] compared to the JJAS climatology, and (right) fraction of the JJAS total precipitation. In brackets at the top of each panel, values and fraction of the peak precipitation anomaly to the west of the black crosses. Only values in a 15^{o} latitudinal band around the maximum of the meridional wind variance (see Figure 7) are displayed.

Figure 9: Fast Fourier transform analysis of grid-point JJAS daily (a) precipitation and (b) meridional wind at 700 hPa, averaged over [5°-16°N, 10°W-10°E] for the CTL and PSRD simulations and [5°-28°N, 10°W-10°E] for the GSRD and GSPD simulations.

Figure 10: JJAS clear-sky SW radiation net flux [W/m^2] at (left) TOA and (right) surface: (1st-3rd row) differences between the sensitivity experiments and the CTL simulation, (4th row) GSRD-GSPD difference. Significance at 95% confidence level is displayed. Radiation is represented as 24-h means, positive values indicate downward net flux. The black rectangle represents the domain where the change in land cover is applied in the Green Sahara experiments. Blue contours display the dust column concentration anomaly in the reduced dust experiments (contours at -2, -1.5, -1, -0.5 mg/kg; see Figure 1b).

Figure 11: JJAS surface (left) sensible and (right) latent heat flux [W/m^2]: (1st-3rd row) differences between the sensitivity experiments and the CTL simulation, (4th row) GSRD-GSPD difference. Significance at 95% confidence level is displayed. Positive values indicate downward flux.

899 Figure 12: JJAS moist static energy [kJ/kg], averaged between 15°W and 25°E: (a-c)
900 differences between the sensitivity experiments and the CTL simulation are displayed in
901 panels, and (c) GSRD-GSPD difference. Significance at 95% confidence level is displayed.
902

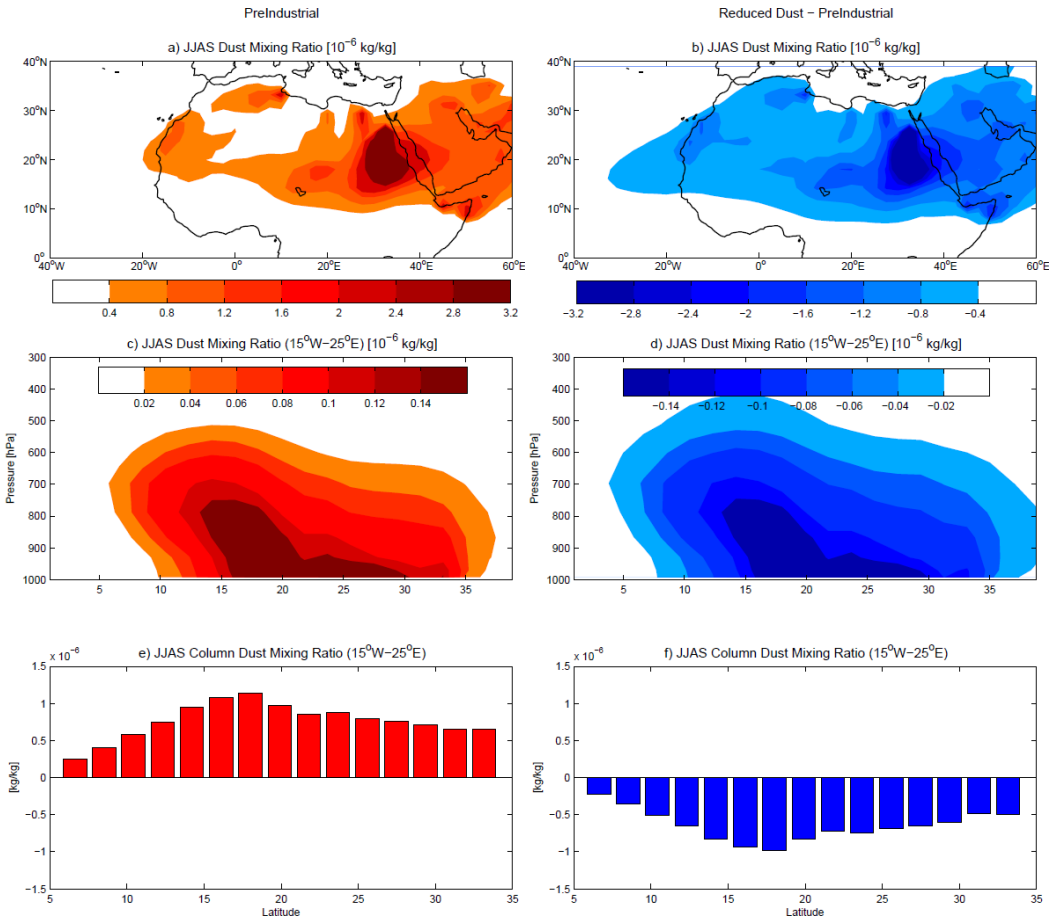

903

904 Figure 1: (left) JJAS pre-industrial dust mixing ratio [kg/kg], prescribed in the CTL and

905 GSPD simulations, and (right) difference between reduced dust and pre-industrial

906 concentration. (a, b) Column integral, (c, d) vertical profile averaged in the range [15°W,

907 25°E], (e, f) meridional profile of the column integral.

908

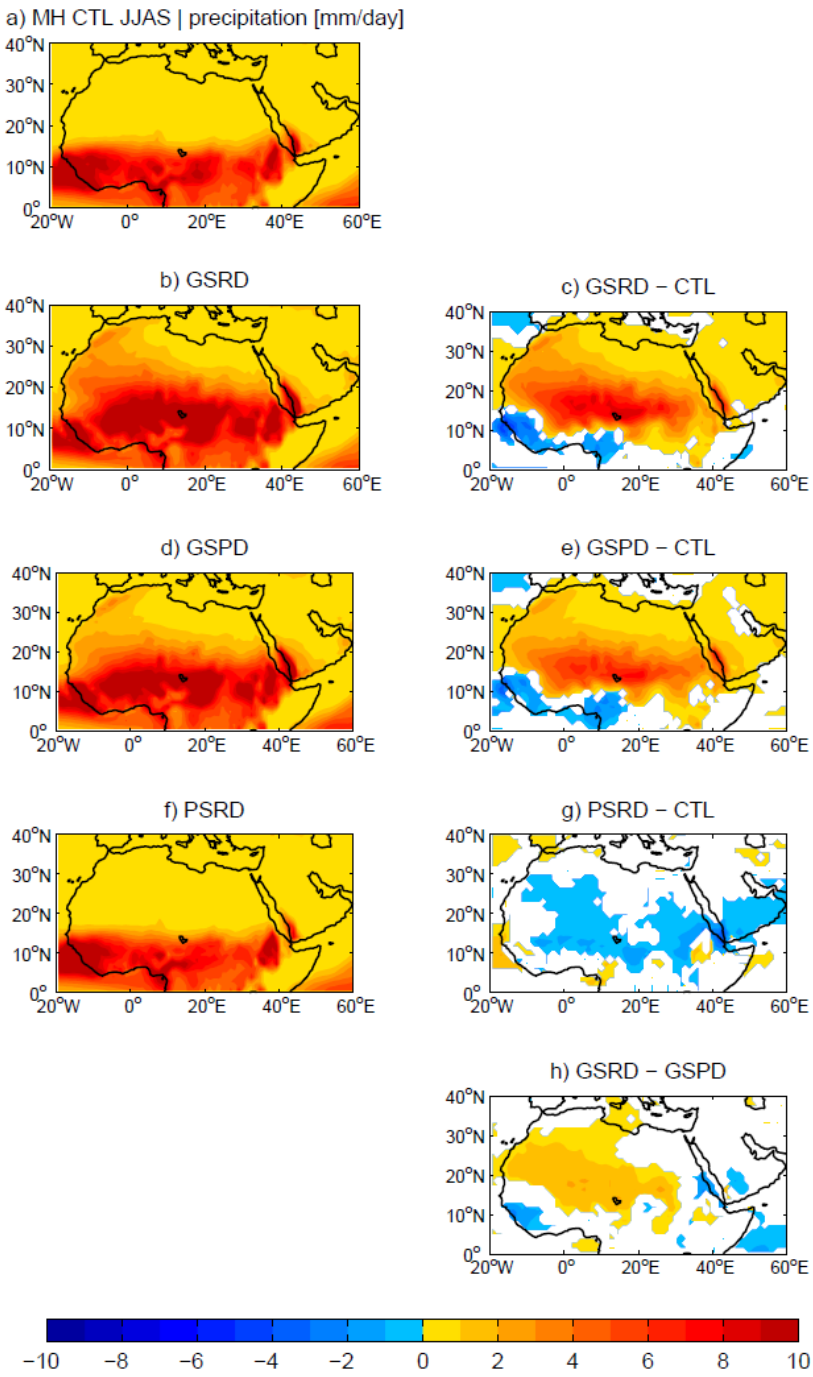

Figure 2: JJAS precipitation [mm/day]: (left) climatological means for the CTL simulation and the sensitivity experiments, and (right) differences between the sensitivity experiments and the CTL simulation. In panel (h), the difference between the GSRD and GSPD experiments is shown. Significance at 95% confidence level is displayed.

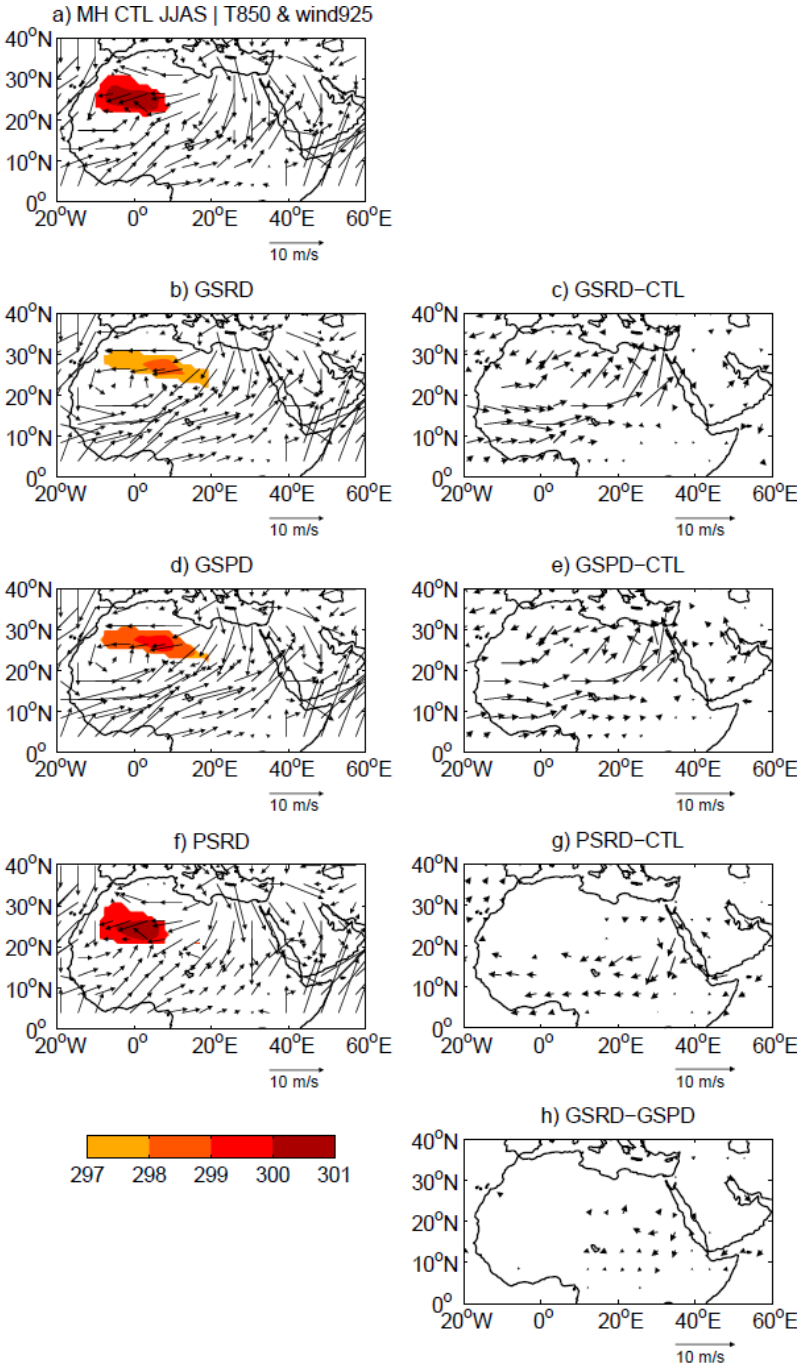

915

916 Figure 3: JJAS wind field at 925 hPa [m/s]: (left) climatological means for the CTL
917 simulation and the sensitivity experiments, and (right) differences between the sensitivity
918 experiments and the CTL simulation. In panel (h), the difference between the GSRD and
919 GSPD experiments is shown. Significance at 95% confidence level is displayed. Shadings
920 indicate the Saharan heat low location and intensity, represented through the values of air
921 temperature at 850 hPa [K] exceeding the 90th percentile in the domain [0-40°N, 20°W-

20°E] [Lavaysse et al., 2009]. The SHL position and intensity is determined by detecting the maximum of the air temperature at 850 hPa inside the domain.

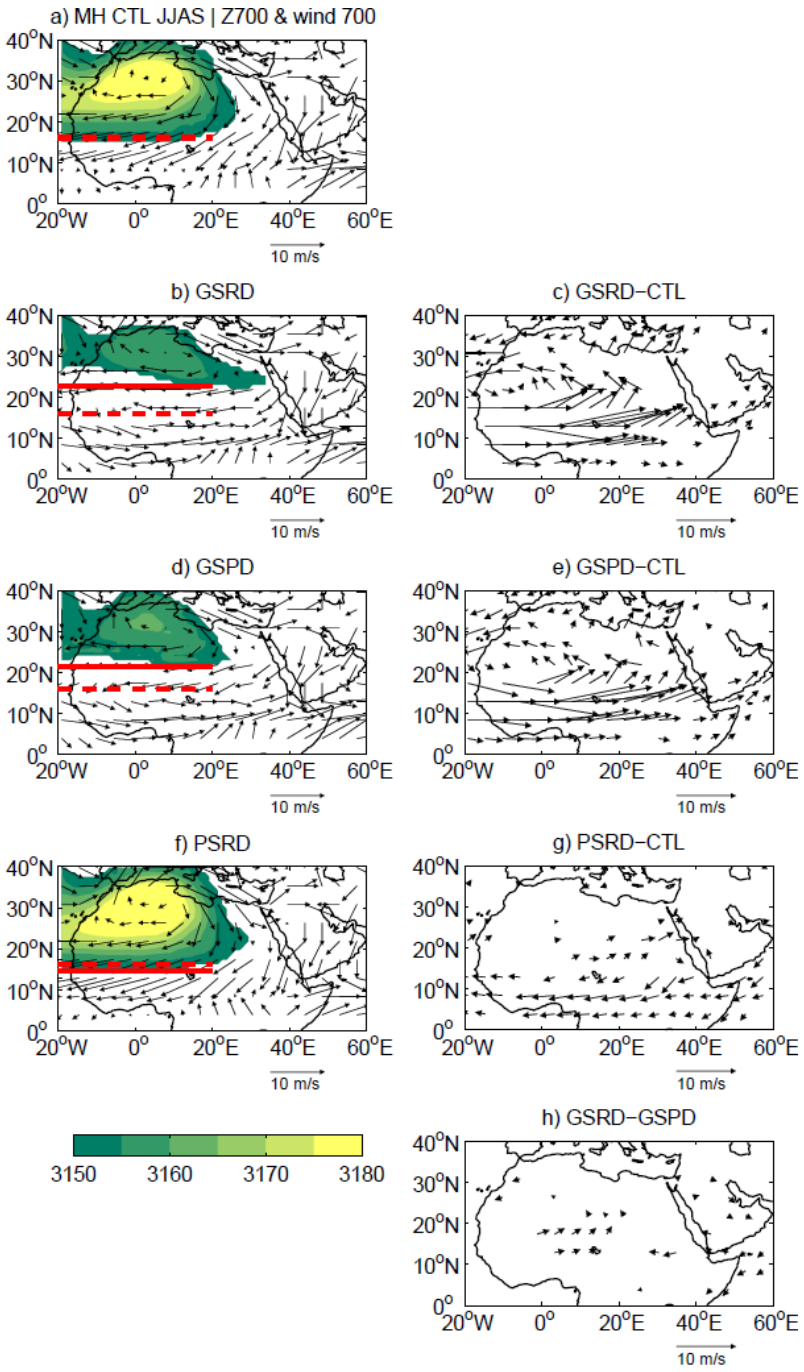

925

926 Figure 4: JJAS wind field at 700 hPa [m/s]: (left) climatological means for the CTL
927 simulation and the sensitivity experiments, and (right) differences between the sensitivity
928 experiments and the CTL simulation. In panel (h), the difference between the GSRD and
929 GSPD experiments is shown. Significance at 95% confidence level is displayed. Shadings
930 indicate the Saharan high location and intensity, represented through the geopotential height
931 at 700 hPa exceeding 3150 m. Red lines represent the mean positions of the African easterly

jet in the CTL simulation (dashed) and the sensitivity experiments (solid). The mean axis of the African easterly jet is determined in the domain [20°W-20°E, 0°-40°N] by detecting, at each longitude, the latitudinal location of the minimum of the zonal wind at 700 hPa, and averaging along the zonal direction.

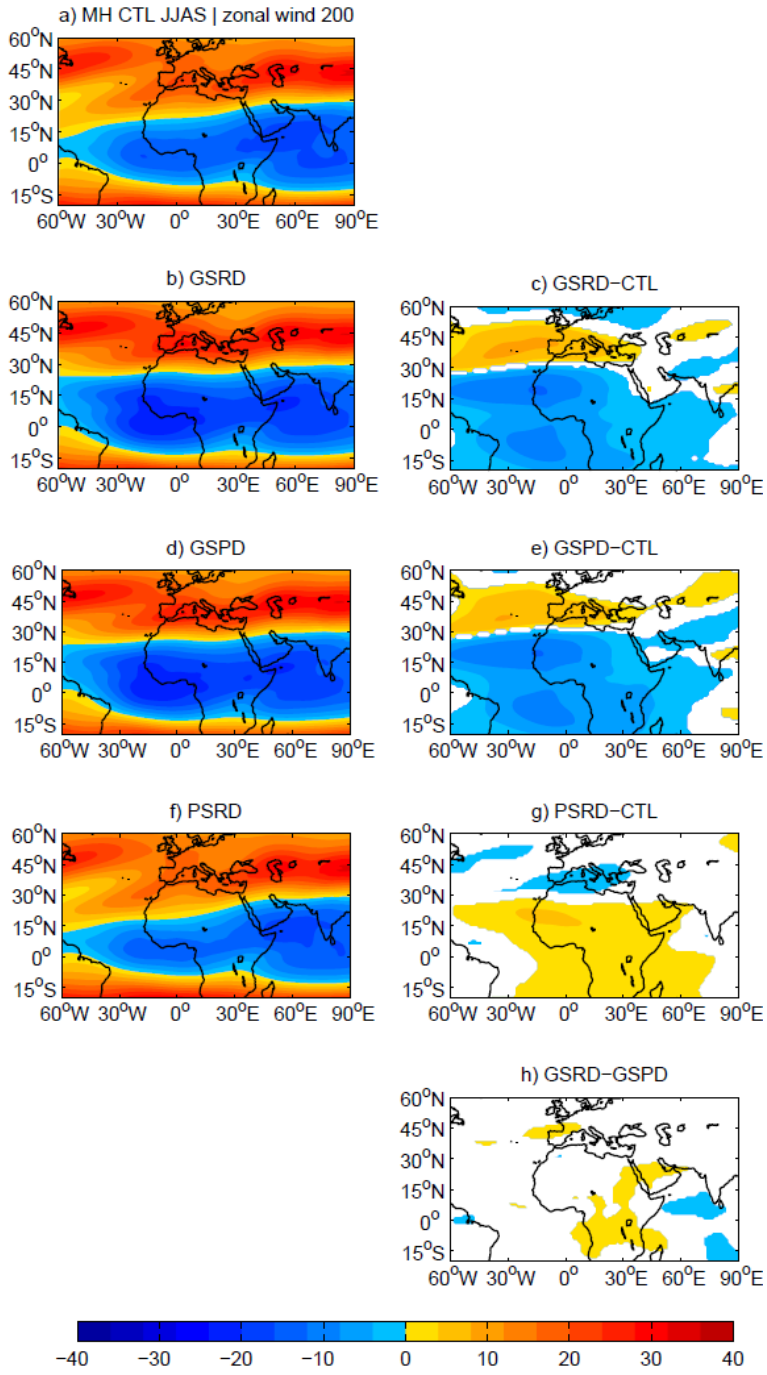

937

938 Figure 5: JJAS wind field at 200 hPa [m/s]: (left) climatological means for the CTL

939 simulation and the sensitivity experiments, and (right) differences between the sensitivity

940 experiments and the CTL simulation. In panel (h), the difference between the GSRD and

941 GSPD experiments is shown. Significance at 95% confidence level is displayed.

942

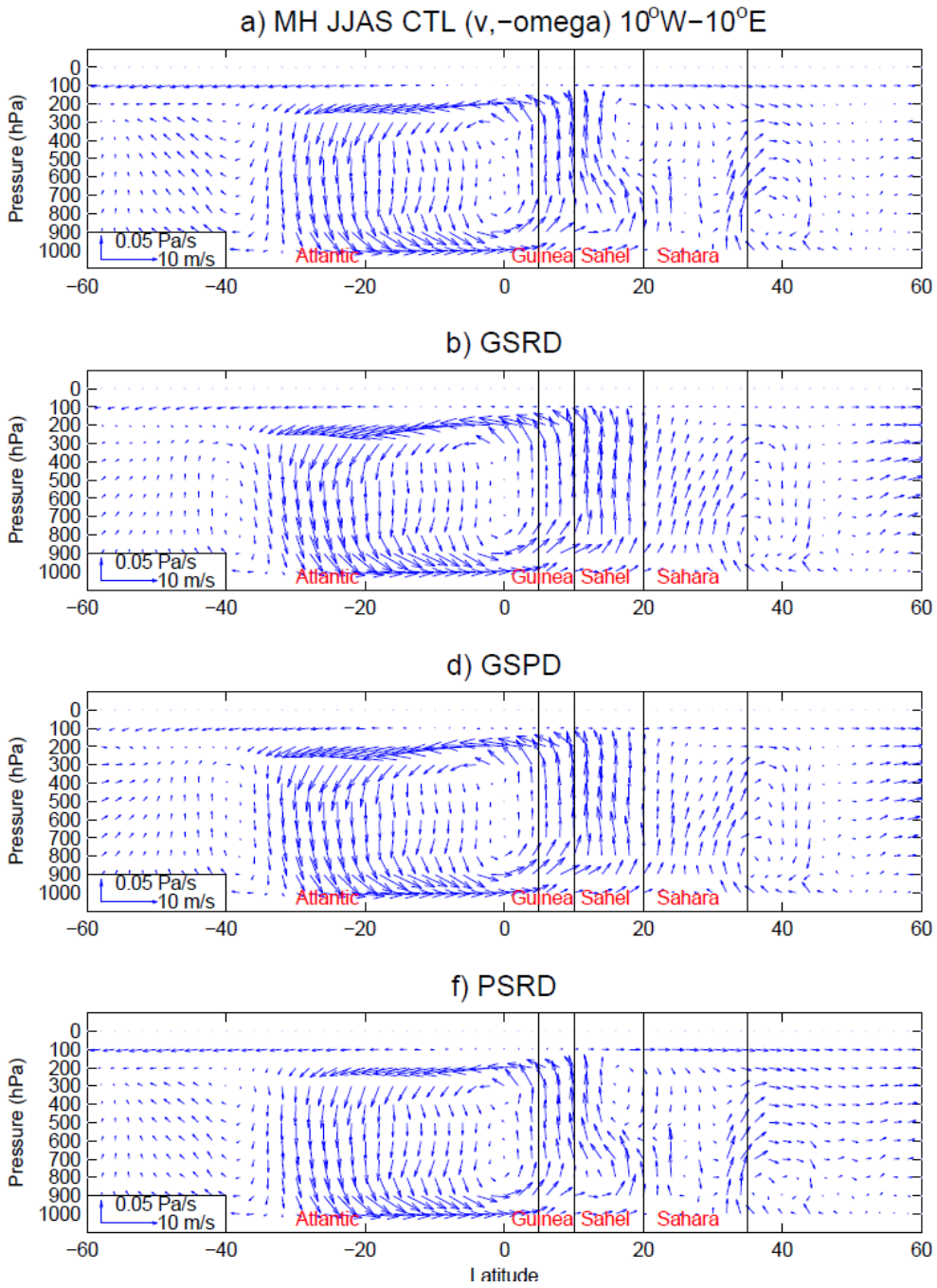
a) MH JJAS CTL (v,−omega) 10°W−10°E
b) GSRD
d) GSPD
f) PSRD
Pressure (hPa)
0
100
200
300
400
500
600
700
800
900
1000
0.05 Pa/s
10 m/s
Atlantic
Guinea
Sahel
Sahara
−60
−40
−20
0
20
40
60
Latitude

943

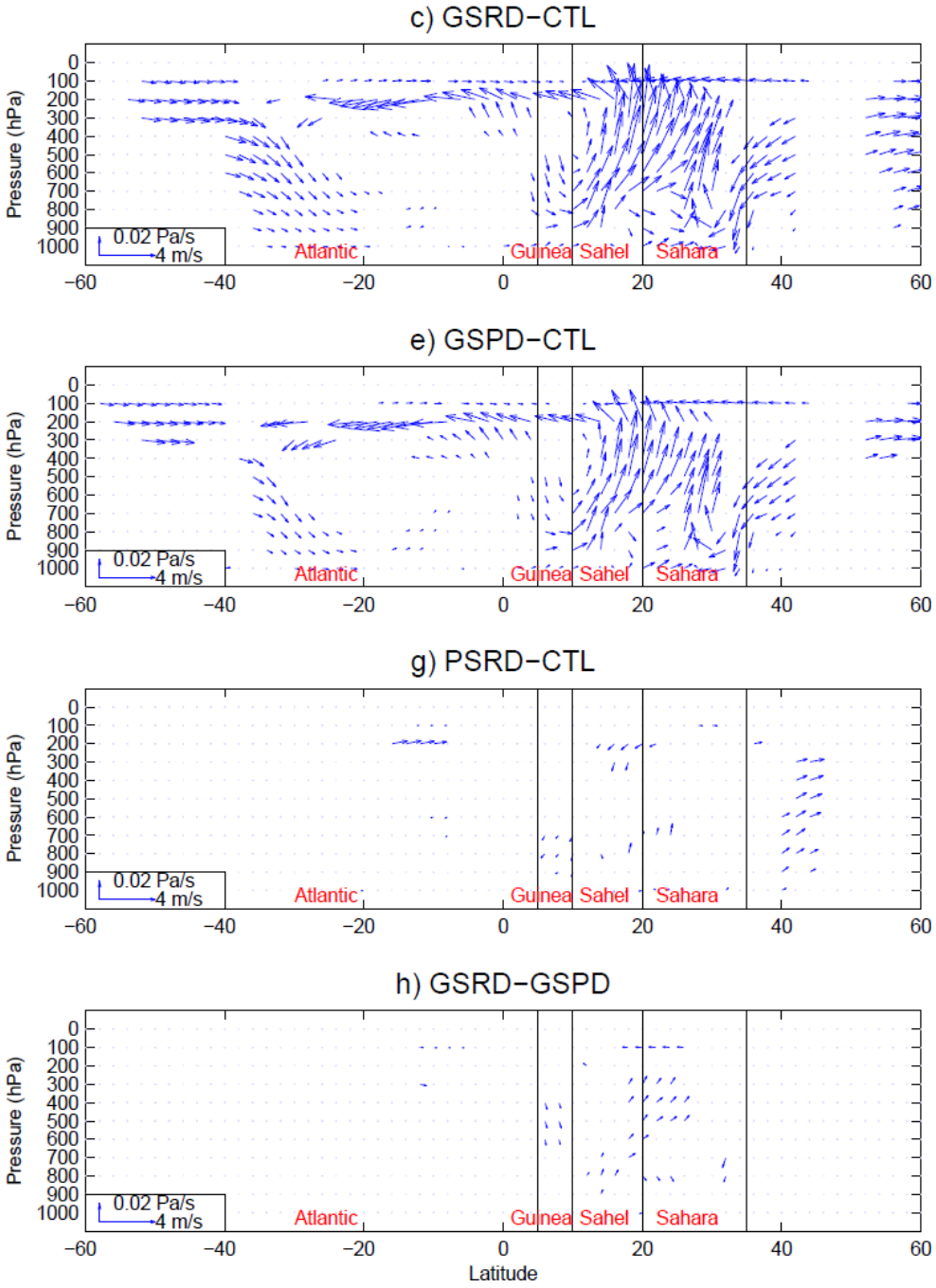

Figure 6: JJAS meridional overturning circulation, represented through the meridional wind [m/s] and the vertical velocity [Pa/s], averaged in the range [10°W, 10°E]: (left) climatological means for the CTL simulation and the sensitivity experiments, and (right) differences between the sensitivity experiments and the CTL simulation. In panel (h), the difference between the GSRD and GSPD experiments is shown. Significance at 95% confidence level is displayed.

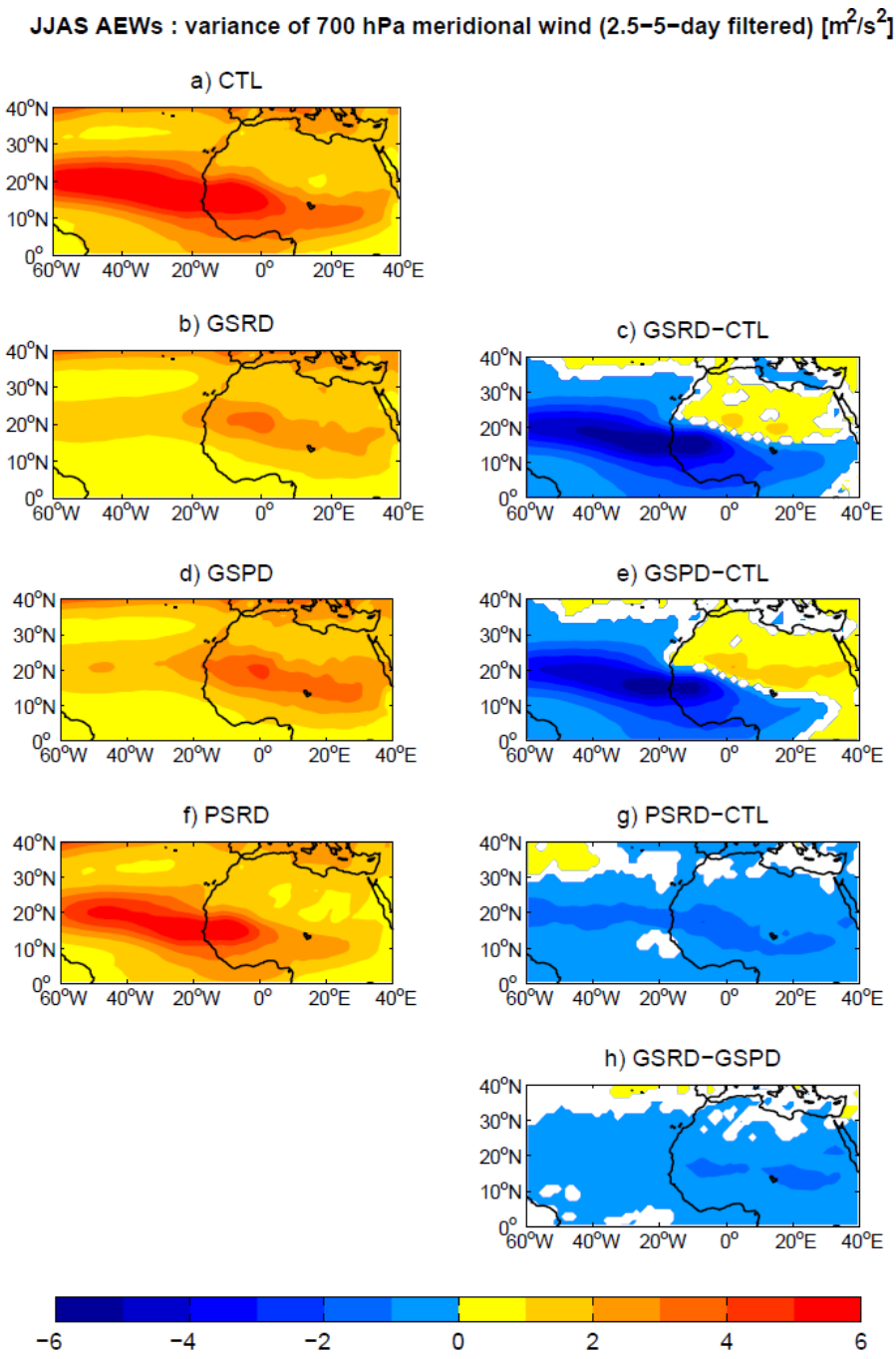

Figure 7: JJAS African easterly wave activity, represented through the variance of the meridional wind at 700 hPa filtered in the 2.5-5-day band [m^2/s^2]: (left) climatological means for the CTL simulation and the sensitivity experiments, and (right) differences between the sensitivity experiments and the CTL simulation. In panel (h), the difference between the GSRD and GSPD experiments is shown. Significance at 95% confidence level is displayed, computed by using a two-sample F test.

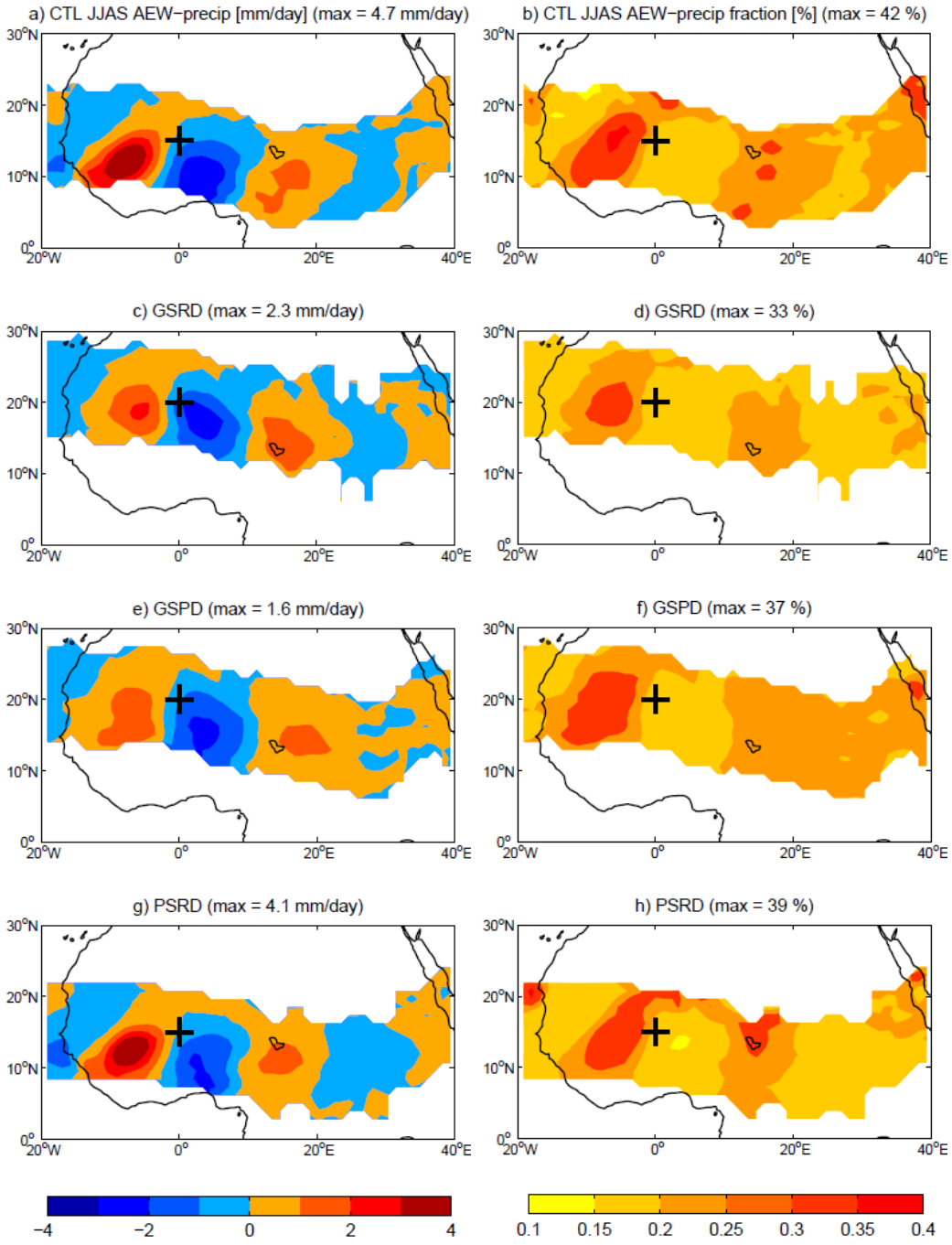

960

961 Figure 8: Precipitation associated with the African easterly waves detected in JJAS at
962 locations indicated by black crosses: (left) precipitation anomalies [mm/day] compared to the
963 JJAS climatology, and (right) fraction of the JJAS total precipitation. In brackets at the top of
964 each panel, values and fraction of the peak precipitation anomaly to the west of the black
965 crosses. Only values in a 15° latitudinal band around the maximum of the meridional wind
966 variance (see Figure 7) are displayed.

967

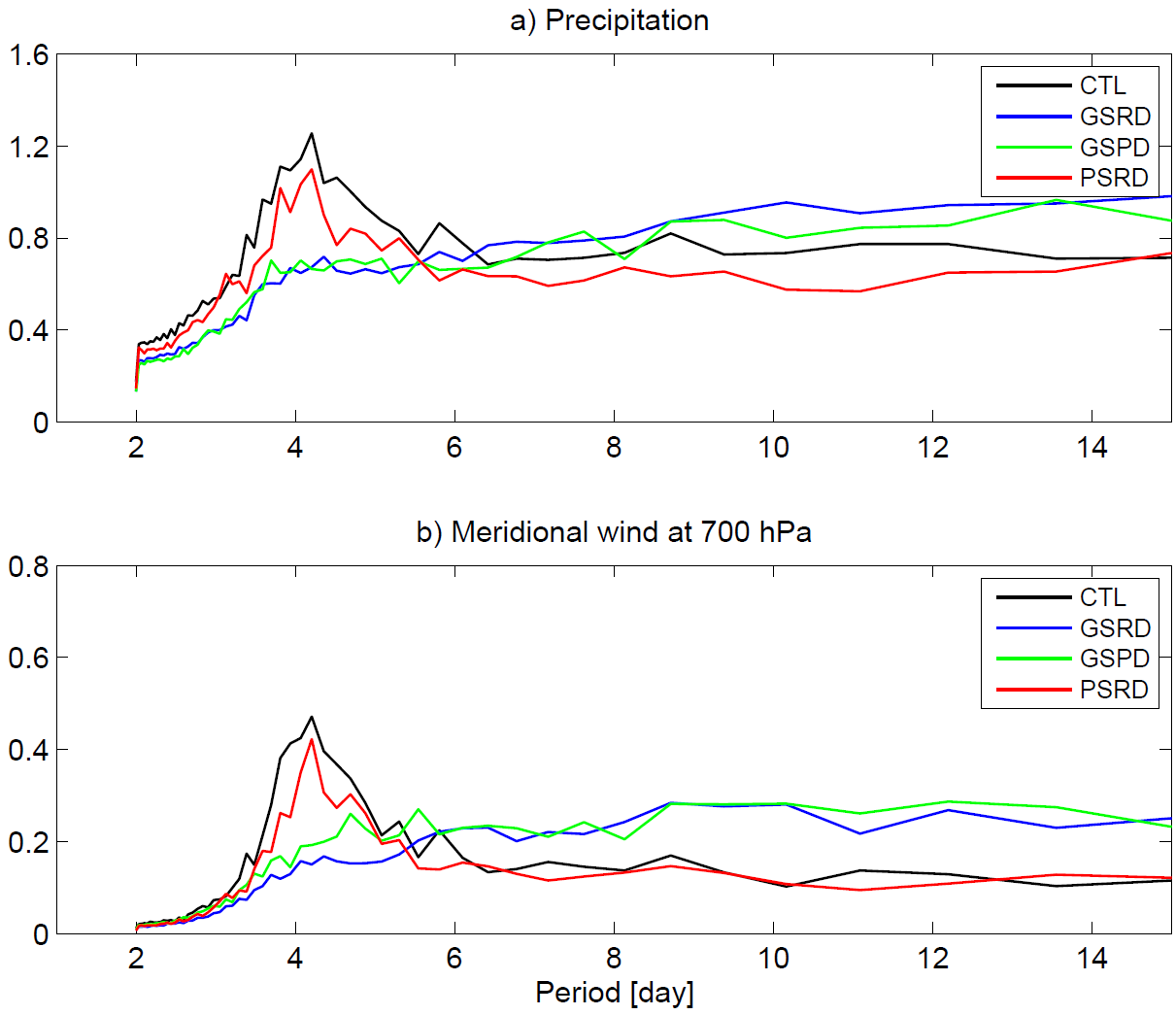

Figure 9: Fast Fourier transform analysis of grid-point JJAS daily (a) precipitation and (b) meridional wind at 700 hPa, averaged over [5°-16°N, 10°W-10°E] for the CTL and PSRD simulations and [5°-28°N, 10°W-10°E] for the GSRD and GSPD simulations.

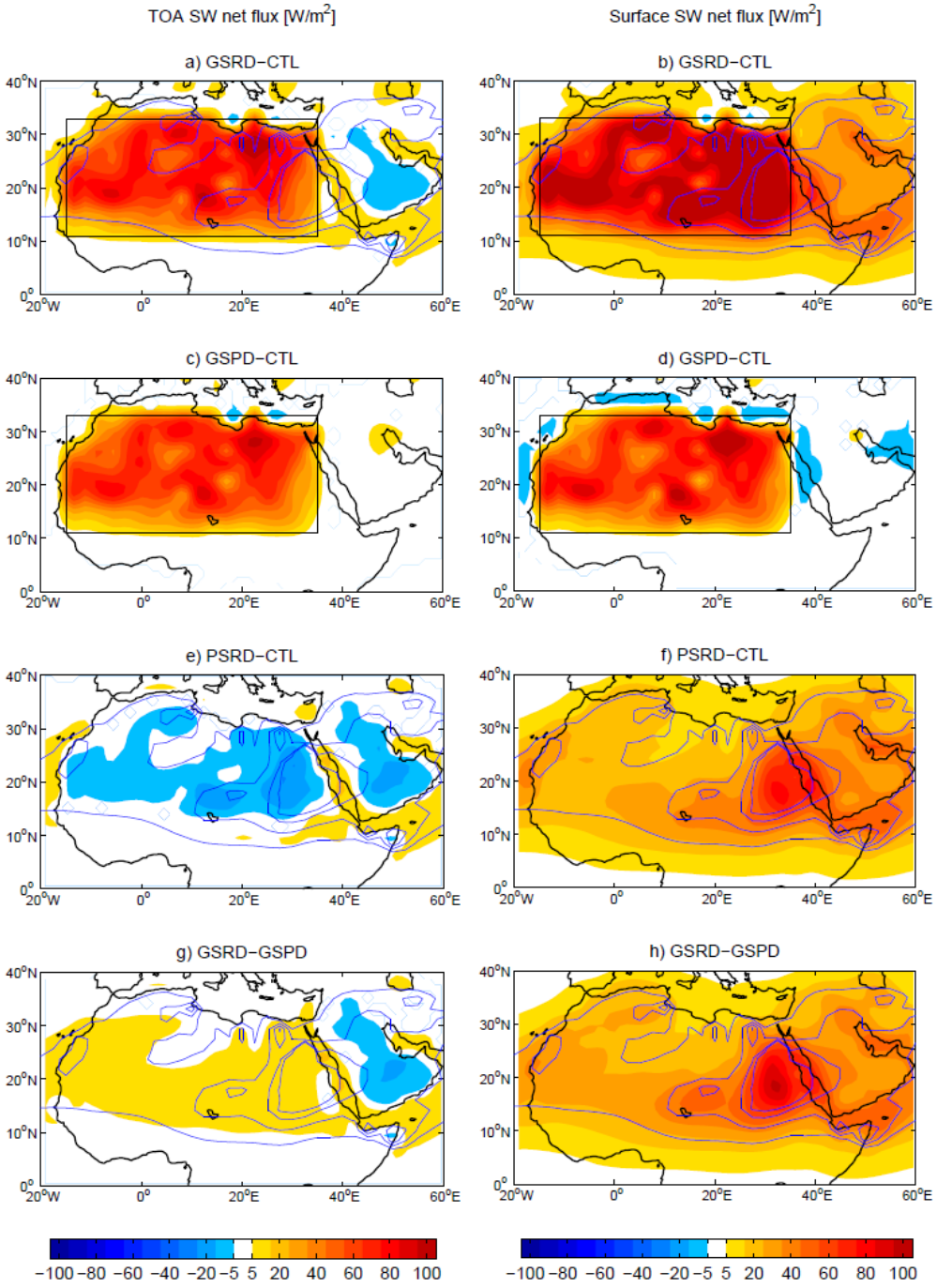

973

974 Figure 10: JJAS clear-sky SW radiation net flux [W/m^2] at (left) TOA and (right) surface:
975 (1st-3rd row) differences between the sensitivity experiments and the CTL simulation, (4th
976 row) GSRD-GSPD difference. Significance at 95% confidence level is displayed. Radiation
977 is represented as 24-h means, positive values indicate downward net flux. The black rectangle
978 represents the domain where the change in land cover is applied in the Green Sahara

979 experiments. Blue contours display the dust column concentration anomaly in the reduced
980 dust experiments (contours at -2, -1.5, -1, -0.5 mg/kg; see Figure 1b).
981

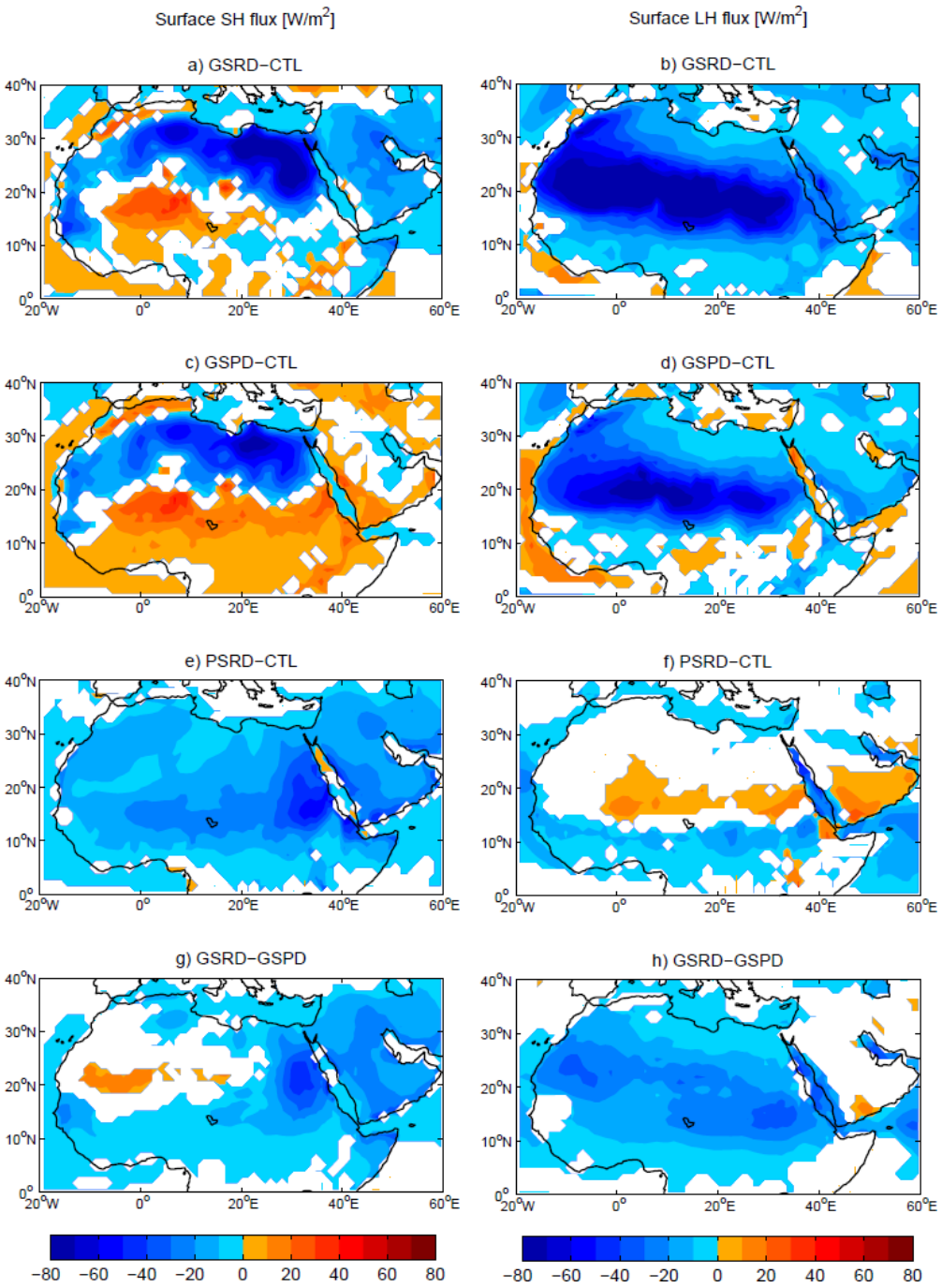

982

983 Figure 11: JJAS surface (left) sensible and (right) latent heat flux [W/m^2]: (1st-3rd row)

984 differences between the sensitivity experiments and the CTL simulation, (4th row) GSRD-

985 GSPD difference. Significance at 95% confidence level is displayed. Positive values indicate

986 downward flux.

987

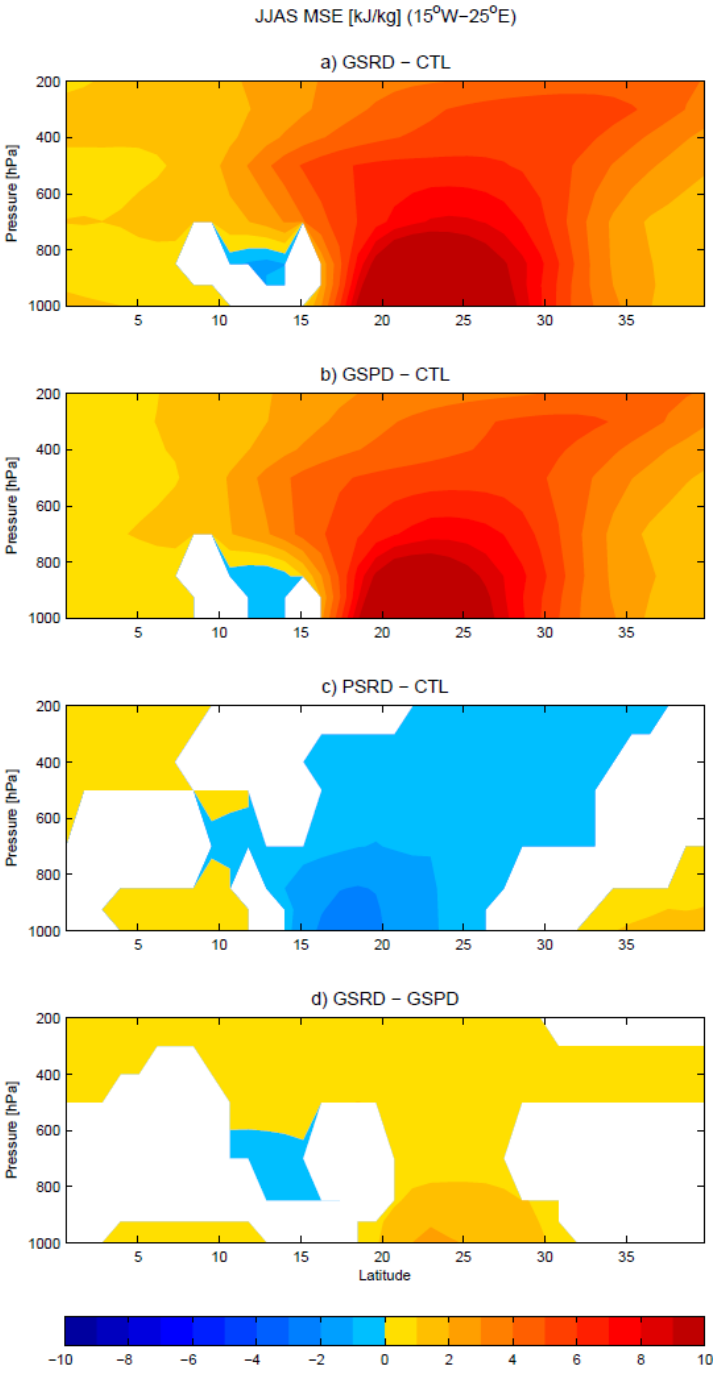

988

989 Figure 12: JJAS moist static energy [kJ/kg], averaged between 15°W and 25°E: (a-c)

990 differences between the sensitivity experiments and the CTL simulation are displayed in

991 panels, and (c) GSRD-GSPD difference. Significance at 95% confidence level is displayed.

992